POLITECNICO
MILANO 1863

Preliminary studies on heavy metals accumulation at nano-scale in the shell of *Patella caerulea*

TESI DI LAUREA MAGISTRALE IN
ENGINEERING PHYSICS - INGEGNERIA FISICA

Author: **Federico Castelli**

Student ID: 970796
Advisor: Prof. Giacomo Claudio Ghiringhelli
Co-advisors: Madeleine Han
Academic Year: 2022-23

Abstract

Mollusks, and in particular the shell structure, are highly sensitive to environmental conditions, making them a valid subject for biomonitoring studies. Different alterations are observed in these living organisms after exposure to a polluted environment, such as structural and chemical alterations of the shell. In particular, chemical alterations typically involve accumulation of trace metals in the shell structure, which is thought to be an excretion mechanism exploited by the mollusk to reduce toxicity in the soft-tissues. The chemical composition of the shell is thus exploited as a valid parameter for assessing water quality, providing a direct proof for the presence of contamination. The vast majority of the studies analyze the chemical composition of the whole shell, without spatially resolving the distribution of chemical elements. Few studies reported the chemical composition resolved at μ-scale, but considering only the major constituents of the shell. The present study proposes a nano-scale spatially resolved analysis of different samples of *Patella caerulea* by means of nano-XRF and nano-tomography, performed at the European Synchrotron Radiation Facility, in Grenoble, France. Nano-XRF technique is employed to determine the chemical composition of different regions of the shell, considering both major constituents and trace metals. Nano-tomography analysis would possibly reveal local changes of density in the shell structure correlated to the presence of trace metals, providing a complementary technique with respect to XRF. The high spatial resolution provided by both techniques would possibly provide further insights, clarifying the way trace metals incorporate in the shell structure and in which regions they accumulate; a topic poorly documented in literature.

Keywords: mollusks, bioaccumulation, pollution, trace metals, XRF, tomography

Sommario

I molluschi, ed in particolare la conchiglia, sono altamente sensibili alle condizioni ambientali, rendendoli validi soggetti per studi di biomonitoraggio ambientale. Differenti alterazioni sono state osservate in questi organismi viventi in seguito ad esposizione ad inquinamento ambientale, come alterazioni strutturali e chimiche della conchiglia. In particolare, alterazioni chimiche tipicamente coinvolgono l'accumulo di tracce di metalli nella struttura della conchiglia, considerato un meccanismo di escrezione impiegato dal mollusco per ridurre la tossicità nei tessuti molli. La composizione chimica del guscio viene quindi impiegata come un valido parametro per valutare la qualità dell'acqua, fornendo una prova diretta della presenza di inquinamento. La stragrande maggioranza degli studi analizza la composizione chimica dell'intera conchiglia senza risolvere spazialmente la distribuzione degli elementi chimici. Pochi studi hanno riportato la composizione chimica risolta su micro-scala, ma considerando soltanto i maggiori costituenti della conchiglia. Il presente studio propone un'analisi risolta spazialmente su scala nanometrica di diversi campioni di *Patella caerulea*, mediante nano-XRF e nano-tomografia. L'analisi è stata svolta al European Synchrotron Radiation Facility, a Grenoble, Francia. La tecnica nano-XRF è stata impiegata per determinare la composizione chimica di differenti regioni della conchiglia, considerando sia i maggiori costituenti che la presenza di tracce di metalli. L'analisi mediante nano-tomografia potrebbe invece rivelare variazioni locali di densità nella struttura della conchiglia correlati alla presenza di metalli, dunque rivelandosi una tecnica complementare a XRF. L'elevata risoluzione spaziale fornita da entrambe le tecniche potrebbe fornire ulteriori informazioni, chiarendo in quale modo i metalli vengono incorporati nella conchiglia e in quali regioni si accumulano; un argomento fino ad ora poco documentato in letteratura.

Parole chiave: molluschi, bioaccumulazione, inquinamento, metalli minori, XRF, tomografia

Contents

1 | Seashells and pollution

Studies on mollusks provide different information about the surrounding environment where these living organism grow. As an example, paleoclimatology studies [1], with the aim of reconstructing the climate of the past, analyze composition of fossil shells with particular interest in oxygen isotope composition, to obtain information concerning temperature changes throughout the past. A different topic, concern the possibility of assessing the level of pollution of water considering the tendency of mollusks to absorb trace elements. Indeed, a polluted environment gives rise to observable effect such as alterations of the shell structure, together with modifications of the chemical composition of both soft-tissues and the shell, making these parameters a valid proxy for biomonitoring the water quality.

In order to better understand the reason which makes these organisms suitable for biomonitoring studies, an overall introduction to the realm of mollusks is presented in section 1.1, providing an overview on the anatomy of these organisms. A specific focus is addressed on the compartments involved in the growth of the shell structure. This protective calcified layer that characterize the vast majority of mollusks, grows through an active process guided by the mollusk itself, belonging to the wider class of biomineralization processes, described in details in section 1.2. The fundamental constituents needed formation of the outer calcified layer are incorporate from the surrounding environment, following different pathways. Inevitably, this leads to the incorporation of other minor elements and trace metals, as discussed in section 1.3, influencing the growth of the mollusk. Other environmental conditions such as water temperature, salinity and pH, influences the growth the mollusk as well. Thus, studying these living organisms provide different information about the surrounding environment, as shown by different studies reported in section 1.5. In particular, highly polluted geographical areas such as the Gulf of Gabes can benefit from the exploitation of this powerful tool, to constantly monitor the sea water conditions. A topic discussed in section 1.6. Nevertheless, the way trace metals incorporate in mollusks, and specifically in the shell structure is still poorly documented in literature. Further analysis employing nano-XRF and nano-tomography on samples collected from the Gulf of Gabes, will possibly provide further insights into the bioaccumulation mechanism, as

introduced in section 1.7.

1.1. Anatomy of mollusks

Mollusks are soft-body animals characterized by the ability to form an outer rigid calcified layer of $CaCO_3$ which protects the living organism from predation and desiccation [2]. Apart from some exceptions for which this protective exoskeleton is lacking, two main polymorphs of $CaCO_3$ can be found in seashells, namely calcite and aragonite. They are usually present in different regions of the shell and can be found in different microstructure arrangement. In the rarest cases vaterite, the least thermodynamically stable polymorph, can be found as well. The shell structure is characterized of different calcified layers of calcium carbonate stacked one on top of the other, usually from 2 to 5 with an additional outer organic layer, the periostracum, better discussed in the following. The stacking of different layers with different microstructures is a mechanism exploited by the mollusk to increase both toughness and flexibility of the shell, reducing the occurrence of fractures. For instance, the vast majority of bivalve mollusks are characterized by two calcified layer, each one providing different advantages to the overall mechanical properties of the shell structure. As reported for the bivalve *Unio Pictorium* [2], the inner layer showed a nacreous aragonitic composition, characterized by small tablets of $CaCO_3$ stacked on top of each other. This microstructural arrangement is known to provides high strength to the shell, even though it lacks of flexibility, with the tendency of cracking when bent. The outer layer in *Unio Pictorium* is instead characterized by aragonitic elungated crystals, disposed perpendicularly to the shell surface, thus named prismatic layer. The presence of this layer on top of the nacreous inner layer provide the lacking flexibility to the overall shell structure. Moreover, the interfaces between different calcified layers avoid cracks propagation through the width of the shell, incrasing the overall mechanical properties of this protective structure.

1.2. Biomineralization process for shell formation

The formation of the shell enters in the wider category of biomineralization processes, namely the process involving formation of minerals by a living organism. Even though the biomineralization process is not fully understood yet, the main mechanisms involved in such a process will be introduced in the following, referring to the work of some authors [2, 3] who tried to outline a general valid scheme applicable to all phyla with minor differences depending on the specific phyla and the species considered.

At larval stage of the mollusk, an organic proteinaceous layer, the periostracum, provides a first template for the formation of the calcified shell structure [2]. The periostracum provides other important advantages to the living organism throughout its life, such as an efficient camouflage against predation and reduction of the shell degradation by fouling organisms [4] which live on the seashell surface. The process of shell formation is governed by the mantle, an organ placed in contact with the inner surface of the shell, which is capable of providing all the macromolecular and ionic ingredients for the synthesis of the shell [2]. During the whole life of the organism the growth of the soft-body requires a simultaneous growth of the shell structure and this occur in concomitance of the outer edges of the living organism, where the periostracum is constantly secreted, and together with the mantle and the shell itself, delimitate a confined space known as extrapallial space, where the precurors of $CaCO_3$ can react forming this compound. A schematic representation of the anatomy of the mollusk, mainly focusing on the compartments involved in the biomineralizatin process, is reported in Figure 1.1. As can be notice from this representation, the extrapallial space is present all along the shell structure, and not only in concomitance of the outer edges, thus allowing a continuous growth in thickness of the shell, throughout the whole life of the mollusk.
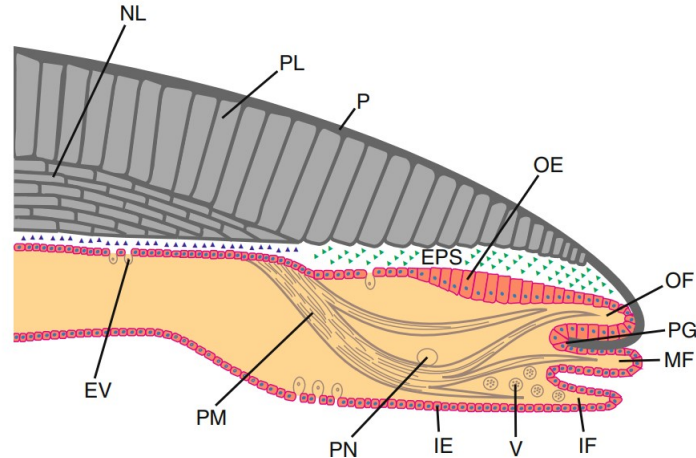
Figure 1.1: Schematic representation of the main compartments involved in the biomineralization process for a bivalve, taken from Kocot et al. [5]. The gray regions represent the shell structure, while the pink region represents the mantle. Green and blue triangles depict organic macromolecules secreted by the mantle and released in extrapallial space. NL: nacreous layer. PL: prismatic layer. P: periostracum. PG: periostracal groove. EPS: extrapallial space. OF: outer fold. MF: middle fold. IF: inner fold. OE: outer epithelium. IE: inner epithelium. PN: pallial nerve. PM: pallial muscle. V: vesicles. EV: exosome-like vesicles.

The extrapallial space is filled with a fluid named extrapallial liquid where a supersat-

uration condition is present for the precursors of calcium carbonate, namely calcium and carbonate ions, as a consequence of a regulation mechanism operated by the organism itself. Moreover, specific concentration and speciation of polysaccharides and proteins in extrapallial liquid are regulated by the organism as well, which both play a crucial role in the biomineralization process, guiding nucleation and formation of the mineral phase.

Without considering the interaction with organic molecules, the calcification process takes place following the general reaction:

$$Ca^{2+} + HCO_3^- \rightarrow CaCO_3 + H^+ \tag{1.1}$$
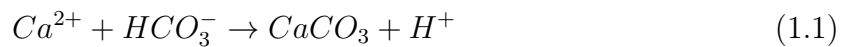
These precursors needed for shell formation are provided by the surrounding environment where the mollusk lives, and three different mechanisms for the uptake of Ca^{2+} into the living organism can be identified. At first, the mollusk can obtain the calcium ions from food, a second mechanism involves the active water filtration activity, and finally, such inorganic precursors can passively diffuse through all parts of the body [2]. Obviously, in terrestrial mollusks it's only the first mechanism that takes place. The other required precursor for $CaCO_3$ formation, i.e., bicarbonate ions, can both derive from CO_2 present in sea water or from CO_2 produced by mitochondria [3].

A detailed description of biomineralization process, which leads from precursors of calcium carbonate to the formation of the crystal structure, could be summarized considering two main complementary mechanism, namely, Particle Attachment (PA) and Ion Attachment (IA), as proposed by Pupa et al. [3].
PA mechanism involves the initial formation of Amorphous Calcium Carbonate (ACC) nanoparticles, justified by the lower supersaturation condition needed for ACC to nucleate, compared to the crystalline phase. ACC particles are formed in intracellular vesicles filled with calcifying fluid, enriched of the precursors of $CaCO_3$. Subsequently, these particles are actively transported to the extrapallial fluid, where aggregate through PA mechanism on the growth surface of the shell, and finally crystallize. The organic molecules present in the extrapallial fluid will give rise to the organic matrix which offer nucleation sites, guiding the crystal growth. Depending on the speciation of the proteins contained in the organic matrix different crystal phase and microstructural arrangement are formed.
On the other side, IA mechanism involves the precipitation of precursor ions present in the extrapallial fluid directly on the growth surface, favored by the supersaturation conditions present in this compartment. The synergistic action of these two mechanisms provide on one side a fast growth of the shell structure by PA, while IA acts as a space-filling mechanism [6] avoiding formation of porosities, which might be detrimental for the mechanical

properties of the shell structure. It's important to stress that these two mechanism contribute in different weights depending on the species considered [3].

1.3. Incorporation of minor elements and trace metals

The ability of mollusks to incorporate the required elements from the surrounding environment lead to the absorption of other chemical elements such as P and S which are fundamental constituents of many proteins, thus of the shell organic matrix. Some minor elements, such as Na^+, K^+, Mg^{2+}, Fe^{3+}, Sr^{2+} [2], are also included in both soft tissues and in the shell structure, in different amounts. Even though the presence of these elements doesn't represent a threat for the organisms in principle, excessive amounts can become toxic. More precisely, as suggested by El-Sorogy et al. [7], both the essentiality and the toxicity of different elements depends on different factors, such as their concentration, the speciation and the form of the element.

Following the same principle, heavy metals can be absorbed and depending on their concentration in the environment this bioacumulation might pose a threaten for the living organism. Elements like Cu, Fe and Zn are considered to be essential elements for marine ecosystem [7, 8], nevertheless, an excessive amount can induce toxicity. For instance, as shown by Lopes-Lima et al. [8], controlled exposure to Cu^{2+} of *Anodonta cygnea* induced morphological alterations both in prismatic and nacreous layer.

Other elements such as Pb, Cr, Cd, Ni, Co are considered hazardous substances harmful for the living organism even at low concentrations [9, 10]. In literature, different mechanisms are suggested as active processes exploited by the mollusks to excrete these hazardous substances. As reported by Lopes-Lima et al. [8], in bivalves, a variety of different sequestration sites are available, such as high-affinity metal binding proteins, granules, calcareous microspheruls and the shell. Considering the shell as one of the main excretion pathways for heavy metals, which is the central topic of the present study, two different main mechanism are suggest by Marin et al. [2] through which the mollusks incorporate heavy metals in the calcified layer.

The first mechanism involves the formation of ACC nanoparticles previously introduced, where heavy metals can be incorporated, afterward, becoming part of the shell structure once ACC particles aggregates through PA. Du et al. [11] confirmed the tendency of biogenic $CaCO_3$ particles to incorporate heavy metals through different mechanisms such as surface adsorption, surface precipitation and ion exchange, supporting this first excretion

mechanism.

The second mechanism guiding the excretion of heavy metals in the shell would involve metal ions absorbed by the mollusk, which are then extruded in the extrapallial space, where a supersaturation condition is reached, with a consequent direct incorporation of these ions in the shell [2], representing a IA mechanism of incorporation. As suggested by different studies, the biomineralization process involving both PA and IA gives rise to an increase of trace elements incorporated in the shell structure compared to IA only. Nevertheless, both PA and IA promote the incorporation of different chemical species. For instance, ACC nucleation occur in smaller volume (i.e., intracellular vesicles) compared to IA which occur in extrapallial space, leading, for example, to an enrichment of Mg, Na and Li together with a depletion of Sr for aragonitic crystals formed by PA more than IA [3].

An additional mechanism for metal accumulation could be identified, similar to the second one proposed. This further mechanism would consider the direct uptake of metallic nanoparticles rather than metal ions. Croteau et al. [12] showed a bioaccumulation of Ag in the soft-tissues after controlled exposure to both Ag^+ and silver nanopartiles, thus corroborating these two last uptake mechanisms proposed.

1.4.   Trace metals accumulation in the periostracum

Bioaccumulation of trace elements might also occur in the outermost layer of the shell, the periostracum. Indeed, the direct exposure of this layer to the marine environment promotes surface adsorption of different chemical elements, such as trace metals. In Zuykov et al. [13] different mollusks were exposed in controlled way to a solution containing Th, observing different tendency of accumulation depending on the structure of the periostracum, which varies from species to species. Accumulation of Pb in the periostracum was observed by Sturesson [14] after controlled exposure of different samples, showing the highest concentration of the metal to be in in this region, compared to the other shell compartments. Other elements like Mn and Fe were shown to be highly accumulated in the periostracum of two freshwater mollusk species by Swinehart et al. [15]. In contrary, a third species of mollusk didn't show any accumulation of these elements in the outer layer, again hinting the accumulation in the periostracum to be species-dependent. Similarly, other heavy metals are expected to accumulate in the periostracum.

The tendency of mollusks to bioaccumulate different chemical elements in different compartments such as soft-tissues, shell structure and periostracum, represent a harmful

situation for the living organism. Indeed, several alterations were reported from mollusks exposed to contaminated water, as will be better discussed in subsection 1.5.2 and subsection 1.5.3. Beside the harmful effects that trace metal exposure might induce, the determination of such alterations provide a valid method for assessing the quality of the water, as will be introduced in next section.

1.5. Biomonitoring seawater quality with seashells

Analysis on both soft-tissues and shell structure of mollusks provide different information about the surrounding environment, in light of the sensitivity of these organisms to environmental conditions. In particular, the presence of contamination can induce structural alterations in the shell, caused by the interference of pollutants with the biomineralization process. Additionally, the tendency of mollusks to incorporate trace elements from the surrounding medium, can lead to alterations of the chemical composition of both soft-tissues and shell itself. The general approach followed for assessing the levels of pollution of sea water by studying mollusks, consider different samples of the same species collected from different areas, among which a gradient of pollution is expected. Alternatively, samples are collected from the same site over a period of time to assess a possible increase or decrease of pollution within the same area [16]. The requirement of selecting and analyzing samples of the same species is necessary in light of the fact that alterations induced by the presence of pollutants, vary from species to species, as will be shown in subsection 1.5.2. Moreover, it's important to notice that shell morphology and chemical composition are influenced by other natural environmental condition such as water temperature, pH, salinity, predation pressure, so that these factors needs to be taken into account to correctly assess the effect of pollution avoiding biases. The main results reported in literature from biomonitoring studies are reported in the following, considering structural alterations in subsection 1.5.2 and chemical composition variations in subsection 1.5.3. Before discussing the results, an overview on the main experimental techniques employed in biomonitoring studies is discussed in subsection 1.5.1.

1.5.1. Experimental techniques for biomonitoring

Two main classes of biominotoring studies can be identified, which focus on different proxies for assessing the effect of water contamination in mollusks. On one side, microstructural and morphometric alterations of shell were reported in different studies as a valid proxy for biominitoring purposes [17, 18]. On the other side, elemental composition alterations of both soft-tissues and the shell structure were successfully exploited in

different studies [16–22]. Nevertheless, the majority of the studies take into account all these parameters in order to achieve more significant results.

A widely employed technique for studying microstructural alterations of the shell is Scanning Electron Microscopy (SEM). This technique exploits an electron beam focused on the sample, to obtain images of the surface of the sample, down to few μm in resolution. Different studies reported a variety of alterations, such as wrong crystallization patterns [8, 18] and presence of surface malformation [16, 19]. SEM could also be employed for assessing morphometric changes, by measuring the shell thickness with high precision [17] thanks to the high resolution achievable, compared to other studies where rulers are employed for such measurements. Structural alterations might also turn into variation of the mechanical properties of the shell, which can be assessed by direct mechanical compression analysis [23]. Similarly, an altered shell structure might be associated to a change in density, as shown by Begliomini et al. [22] where pycnometry analysis were perfomered to measure the shell specific gravity (i.e., the shell density).

In most of the cases, SEM devices provide the possibility to perform Energy Dispersive X-Ray (EDX) analysis as well, which still relies on a focused electron beam to probe the chemical composition of the sample. EDX is known to be only surface sensitive and characterized by an inadequate Low Detection Limit (LOD) for assessing presence of trace metals within the shell structure, in contrary to other techniques. Nevertheless, EDX provides enough information for biomonitoring purposes, where alterations of the concentration of Ca and other minor elements in the shell structure were detected [16–22].

Alternative techniques employed to analyze the chemical composition of the shell are portable-XRF [18], TXRF [21, 22] and Inductively coupled plasma-mass spectometry [7], which are characterized by an improved LOD for trace metals, compared to EDX techniques. Almeida et al. [20] reported a spatially resolved chemical analysis of the shell, performed with Particle Induced X-ray Emission ($PIXE$), distinguishing between the composition of the foliated and the prismatic layer of *Crassostrea gigas*, after controlled Pb exposure in laboratory. Other studies [24, 25] reported the chemical distribution of the main constituents of the shell (Na, P, S) and minor elements (Sr, Mg) obtained by means of, respectively, μ-XRF and X-ray Absorption Near-Edge Spectroscopy ($XANES$), achieving μ-scale spatial resolution, but without any reference to trace metals distribution.

The techniques just introduced provided significant results from different biomonitoring studies, as discussed in the following sections.

1.5.2. Morphometric and microstructure alterations

Both morphometric and microstructural alterations are possibly the most straightforward proxies to be accounted in mollusks for biomonitoring considering the simple techniques required.

A study on Siphonaria Pectinata [18] showed a partial adaptation of this species to a contaminated environment, as suggested by the morphometric and structural alterations observed. Samples were collected from three different sites in Bizerte lagoon (Tunisia), among which a gradient of pollution was expected. The samples coming from the most polluted site showed a shell thickening together with an increase of the weight suggesting that the hardness of the shell was unaffected. Moreover, SEM analysis, showed presence of fibrous inter-beds being thicker and more numerous from the most polluted site. As suggested by different studies [17,18], these inter-beds would provide a shell reinforcement, hinting again a successful adaption to the contaminated environment. Nevertheless, samples exposed to contamination were characterized by a lack of the outer amorphous layer, typically present in this species. Additionally, the median layer was lacking as well, but only in the apex regions of shells coming from the most polluted site. As suggested by this study, the lack of different layers could be the result of exposure to coastal contamination and shipping traffic. Alterations in the crystallization pattern were detected as well, observing the intrusion of the outer layer (whenever present) in the middle one, as a result of a wrong layer integration by the mantle, hinting that pollutants might interfere in the biomineralization process.

Begliomini et al. [22] and Oliveira et al. [23] reported significant structural alterations, together with an increased fragility of the shell structure for the gastropod *Lottia subrugosa*, collected along a contamination gradient over three different sites. More specifically, contaminated samples showed an increased density of the shell structure, possibly resulting from structural alterations of the inner nacreous layer, which increased in thickness. The higher fragility of the shell was suggested to be associated to the decreased thickness of the prismatic layer. The overall reorganization observed of the different calcified layers was related to a protein deficiency. Indeed, as introduced in section 1.1, the organic matrix, mostly composed by proteins, guides the crystallization of the different layers.

Different alterations were reported by Nunez et al. [19] , observing the presence of globular malformations on the inner surface of the shell in *Siphonaria lessoni*, absent in samples from the uncontaminated site. Similar finding were reported by Laitano et al. [16] where inner surface malformation were observed as well. These alterations were observed on the shell inner surface but might also be incorporated into the shell structure during growth. Similarly, Lopes-Lima et al [8] reported malformations on the inner surface of

the shell of *Anodonta cygnea*, related to alterations in the crystallization process. In particular, after controlled exposure of the samples to metal ions (both Cu^{2+} and Cr^{3+}), they observed the presence of an erroneous accelerated precipitation of small crystals in concomitance of the prismatic layer and presence of deep grooves in correspondence of the nacreous layer, when compared to the uncontaminated sample.

Another alteration observed in mollusks exposed to contaminated water was the development of imposex disorder in *Odontocymbiola magellanica* [26] collected from different areas along the east coast of Patagonia, where a high marine traffic was present. Such a disorder leads to a reproductive failure of mollusks, posing a threaten to the proliferation of the species.

The different alterations observed among the studies presented could be accounted considering different parameters. At first, the different alterations observed might be related to the different speciation of the pollutants present in the environment. Secondly, other environmental conditions such as water temperature, salinity and pH must be accounted when comparing different studies. Finally, different species might present different responses after exposure to a contaminated environment, suggesting the need to perform intra-species studies for biomonitoring.

In conclusion, inter-population analysis between samples collected from different sites showed significant results regarding morphological and microstructural alterations, confirming the validity of these parameters for biomonitoring purposes.
An alternative valid method for assessing the levels of pollution of the environment considers the elemental composition of different compartments of the mollusk, as discussed in the following section.

1.5.3.   Elemental composition alterations

Assessing the elemental composition of the shell and metal ions concentration in the soft tissues provide an alternative method for biomonitoring water quality. Analysis performed on soft-tissues prove the effectiveness of this compartment for biominotoring studies [8, 20] . The exploitation of the shell structure for the same purpose provide different advantages compared to soft-tissues as suggested by Cravo et al. [27]: i) shell composition reveals less variability, (ii) it preserves the accumulated elements over the whole life of the mollusk, (iii) and it's more simple to be stored and preserved. Moreover,

analyzing the chemical composition of the shell might help to elucidate the different possible metabolic pathways through which different metals are incorporated in the mollusks, providing a better understanding on how these contaminants lead to the morphometric and microstructural alterations briefly discussed in the previous section. In the following, the main results available in literature concerning elemental composition alterations will be discussed.

As a general trend, a decrease in Ca content was observed following exposure to a contaminated environment [16–22] as summarized in Table 1.1. The values reported ranges from a $\approx 7\%$ decrease observed by Begliomini et al. [22] up to a $\approx 30\%$ decrease reported by Lahbib et al. [17]. A calcium decrease is usually associated to the presence of non-essentials metal ions which can directly compete with the Ca^{2+} uptake as consequence of their similar atomic radius [18]. Other studies suggest calcium content decrease to be associated to contamination-induced alterations of the organic matrix [19] which is responsible, as previously introduced, of the correct $CaCO_3$ deposition. Together with Ca content decrease, S and P content decrease were observed in all previous studies hinting alterations of the organic matrix and thus corroborating the importance of the organic matrix alterations in inducing a Ca reduction. Moreover, organic matrix modifications would be directly related to morphological alterations discussed in subsection 1.5.2, such as formation of globular malformations [16], increased fragility [22] and shell layers remodelling [18].

Control site (%)	Contaminated site (%)	Reference
46.4 ± 3.8	15.2 ± 1.6	*H. trunculus* [17]
42.3 ± 5.6	8.0 ± 1.0	*S. pectinata* [18]
38.0 ± 1	31.1 ± 0.9	*L. subrugosa* [22]
33.0	19.7	*B. odites* [16][*]
27.0	7.0	*S. lessoni* [19][*]

Table 1.1: Ca percentage composition of the shell between control site and contaminated site from different studies. [*] standard deviation was not reported.

Two other abundant elements in the shell are Mg and Si showed an overall increase after pollutant exposure in different studies [17,18,27]. This general trend allows to exploit these elements concentration as a valid parameter for biomonitoring purposes, similarly to the decrease of Ca content previously discussed. Nevertheless, as shown by Lahbib et al. [17], high concentration of these compounds are localized in the periostracum layer as a consequence of microfouling organism, possibly leading to biases especially in those

studies where the chemical composition of the whole shell is evaluated from powdered samples.

A minor element always present in the shell structure is Sr, which can easily substitute with Ca due to its atomic similarity, even though no specific functionalities are reported in literature for this element. Different results are reported in literature concerning the variation of concentration of Sr after contaminant exposure of the mollusk. In two separate studies [18, 20] was observed a decrease of Sr content , in contrary Begliomini et al. [22] observed an increase, suggesting again that different species might respond differently to the presence of contaminants. Thus, studies considering different species belonging to the genus of *Patella* would represent a more significant standard for comparison, considering that the present study relies on samples of *Patella caerulea*, as further explained in section 1.7. Nevertheless, even intra-genus dissimilarity were observed: Cravo et al. [27] reported a decrease of Sr contrarily to the increase observed by Foster et al. [28], for two different species of *Patella*, after contamination exposure. Moreover, as suggested by both studies, the concentration of this compound is influenced by other factors other than water contamination, such as water salinity, making concentrations of Sr a subtle parameter for biomonitoring studies in these species.

Similarly to what was observed for morphometric and structural alterations, there's a high inter-species variability, making difficult to draw an overall trend for some elements like Sr. Other elements, like Ca showed more homogeneous inter-species results.

The presence of non essential trace metals in the mollusk is most likely associated to environmental availability, providing a direct assessment of the water contamination. Different studies [7, 16, 18, 20–22, 27] showed the validity of exploiting chemical analysis for biomonitoring purposes, especially considering trace metals accumulation. Other than that, knowing the chemical composition allows to correlate the structural alterations observed with the presence of different pollutants. In this way, the toxicity of different trace elements can be better clarified.
The highly polluted geographical area of the Gulf of Gabes represent a threat for the marine ecosystem and humans inhabiting the litoral regions. Thus, the techniques introduced in the previous sections provide a powerful and simple tool to constantly check the presence of toxic compounds in this region, possibly preventing harmful situations.

1.6.   Seawater contamination in gulf of Gabes: a case study

The Gulf of Gabes extends for more than 400 km along the east coast of Tunisia and it is recognized as one of the most important fishing areas in Tunisia [9], and one of the most polluted regions of the Mediterranean Sea at the same time [29], thus representing a harmful situation for the marine environment and for humans. The presence of pollution in this area is associated to anthropogenic sources, including harbors, industries and fishing activities, distributed all along the litoral of the gulf. In the present study two different regions in the gulf were considered for assessing the effect of water contamination on seashells.

1.6.1.   Phosphogypsum contamination

A particular concern in gulf of Gabes is due to the large amount of industrial wastes produced from the phosphate fertilizer factories known as the Tunisian Chemical Group (GCT), and directly discharged in the sea water. In concomitance of Gabes city the GCT releases an estimated daily amount of 14400 tons of PhosphoGypsum (PG), the by-product obtained from the production of fertilizers, in form of gypseous water. As reported by Annabi-Trabelsi et al [30] PG would mainly contain gypsum, fluorides, phosphorus, sulfate ions, heavy metals, such as Cd, Cr, Cu, Zn, Pb, As, organic matter and radionuclides. The presence of heavy metals could be directly related to organic matter fraction composing PG, which offer high affinity binding sites where such trace elements can attach [31]. A further concern related to discharges of PG in sea water, as reported by El Zerelli et al. [31], is associated to the formation of a foam named PhosphoGypsum Foam (PGF) which floats on water surface, being capable of transporting the toxic compounds incorporated over several kilometers, depending on wind direction and strength, thus increasing the extension of the area affected by pollution. Annabi-Trabelsi et al. [30] reported a gradient of water contamination along the coast, down to the city of Zarat located at 30 km from Gabes, supporting the spreading of contamination due to PGF. In 2018, a study [31] conducted the first complete characterization of PGF, observing presence of toxic heavy metals, where most of them exceed the Tunisian standard for the discharge of industrial wastewater in marine environment. The element considered and reported in Table 1.2 are those of interest for the present study. Morever, granulometric analysis reported 63% of the total PGF was composed by PGF particles with a diamater smaller than 2 μm suggesting an enhanced bioaccumulation from the surrounding environment.

Trace element	Concentration $(\mu g/g)$
$Fe(wt\%)$	1.99 ± 0.20
$Sr(wt\%)$	0.31 ± 0.03
Zn	1770
Cr	412
Cu	223
Ni	203
Mn	87
Zr	82.4
Cd	49.8
As	30.2
Co	4.6
W	2.3
Sn	1.3
Ge	0.52

Table 1.2: Trace element concentration in PGF collected in the vicinity of Gabes city reported by El Zerelli et al. [31]. The elements considered are only those of interest in the present analysis.

As previously mentioned, PGF floats on the surface of water pushed by the wind, until the mechanical force of waves and hydrodynamics lead to decomposition of PGF, thus releasing toxic elements in the sea water.

1.6.2. Seawater quality in the Gulf of Gabes

Drira et al. [9] reported a chemical analysis regarding presence of trace elements in surface sea water collected from different sites in the Gulf of Gabes in 2014, considering Ni, Fe, Pb, Cu, Cr, Zn, Co, Cd, Mn concentrations. The results obtained largely exceeds the safety limits set by different institutions dedicated to water quality assessment. More specifically, considering the area close to the city of Gabes, high amounts of Zn, Ni, Co and Cd were found. A different study [10] considered four sites along Tunisian coast, showing that the highest concentration of Cu, Cd, Ni, Pb, and Zn were found in the soft-tissues of *Patella caerulea* collected from Gabes. Both Drira et al. [9] and Zaidi et al. [10] related the presence of high concentrations of trace metals to the by-product from phosphate industries discharged into the sea (i.e., PG), even though other sources of heavy metals were suggested in Drira et al. [9]. Additional Pb could be released in the water from spill of petrol by fishing boats. Tanneries along the coast are suggested as

a possible additional source of Cr contamination, even though high concentration of Cr were reported in [31] for PGF composition, possibly being the main responsible for the presence of Cr. Presence of Sn could also be associated to Tributyltin (TBT), a biocide used in antifouling paints on boats. As shown by several studies, TBT pose a threaten for mollusks, leading to shell structural alterations as reported by [18]. Even though TBT was globally banned since 2008, as suggested by a more recent study published in 2016 [32], Sn was still present on boats hull from old layers of antifouling paint made with TBT, covered by other newer layers of anti fouling paint, thus possibly still being released during maintenance work of the boats in the harbor area. Cu and Zn were also present on the boats hull as shown by XRF analysis from this study.

The high pollution levels reported in the gulf of Gabes, and more specifically in the vicinity of Gabes city, represent an adequate area to collect samples exposed to contamination for further chemical analysis.

1.6.3.   Shell samples of *Patella caerulea*

Patella caerulea is a common limpet part of the class of gastropods inhabiting rocky shores along the Mediterranean Sea, which feeds of seaweed and algae [33]. Different studies relied on *P. caerulea* for biomonitoring purposes. Slama et al. [34] considered *P. caerulea* for monitoring TBT contamination. Yüzereroglu et al. [35] showed noticeable chemical composition alterations in the soft-tissues after heavy metal exposure for *P. caerulea*. Nevertheless, no studies concerning heavy metal accumulation in the shell *P. caerulea* were found in literature.

In the present study, samples of *Patella caerulea* collected in September of 2012 from two different areas from the Gulf of Gabes[1] were analyzed for assessing the composition of the shell structure. More specifically, two samples collected from the breakwater in the fishing harbour of Gabes, and one sample collected from the breakwater in the fishing harbor of Zarat, were considered in the present analysis. The first site is considered a highly polluted site in gulf of Gabes, while the harbor area of Zarat represents the control site.

---

[1]Samples were provided by Youseff Lahbib, University of Carthage, Faculty of sciences of Bizerte

1.7. The aim of the present study

The techniques usually exploited in biomonitoring studies (see subsection 1.5.1) are limited in spatial resolution, at most providing chemical analysis at μ-scale. No studies reported the chemical compostion, considering trace metals, with a nano-scale resolution. The present study proposes both nano-XRF and nano-tomography analysis of the shell structure of different samples. Nano-XRF was exploited for analyzing the chemical composition of the shell with nano-scale spatial resolution, at first, with the aim of assessing the average levels of pollution of the samples, and secondly, studying the way trace metals were accumulated in the shell structure. Nano-XRF will possibly provide further insight into bioaccumulation of different heavy metals. Nano-tomography was exploited as a complementary technique for assessing the shell composition, possibly observing inhomogeneity in the shell density, which could be related to localized regions where trace elements accumulate.

The experiments were conducted at ID16B beamline at European Synchrotron Radiation Facility, as will be presented in the following chaper.

2 | Experimental technique

In this chapter will be presented a brief introduction to ESRF research center, mainly focusing on ID16B beamline, where the present study was conducted. A description regarding the experimental techniques exploited (nano-XRF and nano-tomography) will be presented, respectively, in section 2.3 and section 2.4.

2.1. ESRF

Electron Synchrotron Radiation Facility (*ESRF*), after the completion of the Extremely Brilliant Source (*EBS*) project became the first fourth-generation high-energy synchrotron in the world, being capable of producing X-rays 100 billion times brighter than the X-rays used in hospitals [36]. Since it became operational in 1992, several beamlines have been constructed, hosting nowadays 42 [37] different operational beamlines distributed all around the 844 meters in circumference storage ring, where electrons are accelerated to generate synchrotron radiation.

2.1.1. Generation of synchrotron radiation at ESRF

Generation of synchrotron radiation relies on a simple principle of physics: charged particles moving in a curved trajectory emit electromagnetic radiation in a tangential direction. In case of synchrotron radiation generation at ESRF, the charged particles exploited are electrons, which are accelerated to a nominal value of 6Gev into a closed loop path, so that electromagnetic radiation is emitted in a direction tangential to the electrons' orbit.

A simplified scheme of ESRF is reported in Figure 2.1 where four main sections can be identified: the linac system, the booster synchrotron, the storage ring and the beamlines. At first, electrons are linearly accelerated up to 200Mev in linac system. Subsequently, electrons are injected in the booster synchrotron which allows to further accelerate electrons to relativistic velocities (6GeV). The injection system allows to transfer electrons to the storage ring, made of circular evacuated pipes, where the electron beam is finally
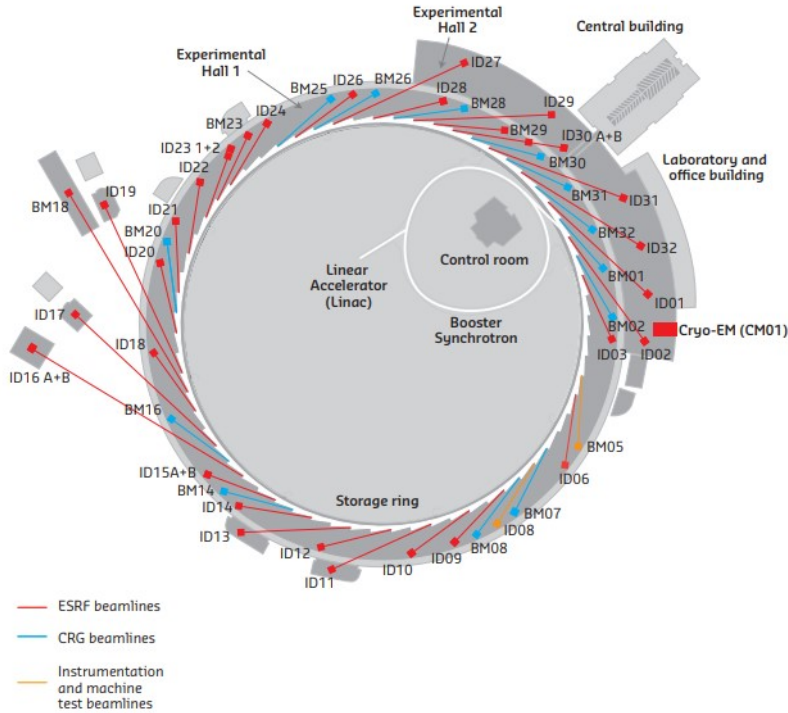
Figure 2.1: Scheme of ESRF linac system, booster synchrotron, storage ring and beamlines [38]

exploited for synchrony radiation generation, by means of bending magnets, undulators and wigglers. Whenever electrons emit radiation they lose part of their kinetic energy, which is then restored up to the nominal value of 6GeV by means of RF cavities distributed along the storage ring. The relativistic velocities of the electrons beam, together with the complex apparatus of bending magnets, undulators and wigglers, give unique characteristics to the emitted radiation such as high intensity, high collimation, broad and continous spectral range, pulsed time structure [39].

2.2. ID16B nanoprobe beamline

ID16B is a hard X-rays nanoprobe beamline [40], where a sophisticated apparatus embodied within a 165 meters long evacuated tube allows high collimation of the X-rays, down to $50 * 50nm^2$ beam spot-size. The small beam spot-size together with the high energy resolution are achieved by the usage of different components placed all along the 165 meters that separate the beam source to the sample stage, as introduced in the following sections. Moreover, the high collimation of the beam over such a long distane requires continuous alignment of the apparatus to ensure a correct focusing of the beam. ID16B provide different nano-scale X-ray techniques such as X-Ray Fluorescence (XRF),

X-ray Diffraction (XRD), phase contrast 3D imaging and so on. The energy range covered ranges from 4.0 keV up to 34keV [41] with an energy resolution down to $\Delta E/E \approx 10^{-4}$.

The beamline can be schematically divided in three sections: the optics hutch, a long evacuated tube and the experimental hutch, as represented in Figure 2.2.
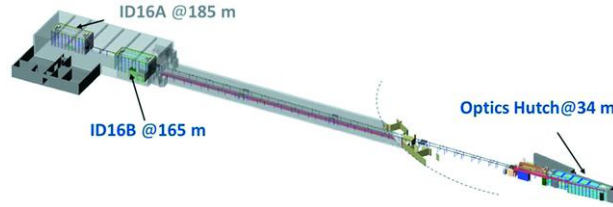

Figure 2.2: Schematic representation of ID16B, from the optics hutch to the experimental hutch.

2.2.1.   Optics Hutch

The optics hutch comprehend, in order, an in-vacuum undulator (CPMU20.5) for X-Rays generation, a double white-beam mirror for harmonic rejection, a Double Crystal Monochromator (DCM), a precision slit for horizontal focusing of the beam, working as a secondary source and different Si and Ge filters to provide the possibility to reduce the beam flux.

The CPMU20.5 works under vacuum at cryogenic temperature (80K), producing a brilliant source of X-rays. Brilliance (or spectral brightness) is defined as the number of photons emitted per second per bandwitdth per unit solid angle and unit area of the source [42]. In Figure 2.3 is shown the brilliance of CPMU20.5 for different energies. Only the first and the third harmonic are effectively exploited for measurements. More specifically, up to $\approx$14 keV the first harmonic provide highest brilliance, while above this energy, the third harmonic is exploited up to 34 keV.

Both the double white-beam mirror and the DCM are located as close as possible from the source, in order to minimize deterioration of coherence of the beam, which is fundamental for both strong focusing and phase contrast imaging technique. Depending on the choice of which of those two devices is made operational, two different modes of operation are possible at ID16B: the monochromatic beam mode at low energies is obtained using both the double mirror and the DCM while the pink beam mode is obtained by removing the monochromator, thus being characterized by a broader energy spectrum. A summary of the main characteristics of these two modes is reported in Table 2.1.

As previously mentioned, the role of the double white-beam mirror is to reject un-
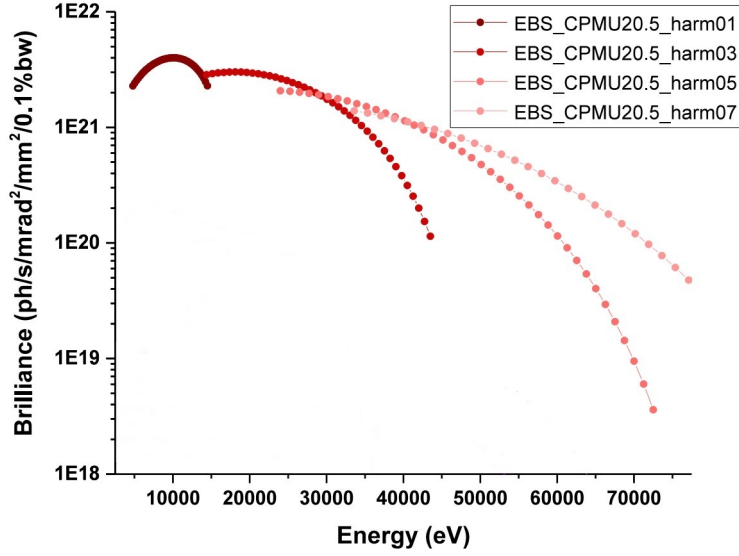
Figure 2.3: Brilliance of CPMU20.5 for different harmonics [40]

Mode of operation	Energy	$\Delta E/E$
Monochromatic low energy	4 - 34 keV	$\approx 10^{-4}$
Pink beam mode	17.5 - 34 keV	$\approx 10^{-2}$

Table 2.1: Two different operating mode at ID16B. Energy resolution values taken from [43].

wanted higher order harmonics. Moreover, such a device provide the possibility to focus horizontally the secondary source generated by the precision slit, which will be better discussed in the following, together with the possibility of tuning the angular beam direction, which is required considering the impossibility of lateral movement of the end-station present in the experimental hutch. The DCM allows to define the X-ray beam energy with high precision and resolution. Moreover, energy scan with excellent repeatability are made possible with the use of such a device.

The working principle at the basis of generation of synchrotron radiation allows a natural high collimation of the emitted radiation along vertical direction [39], which can be directly de-magnified by the insertion device (undulator), in contrary to the wider angular distribution along the horizontal direction. In order to focus the beam along the horizontal direction a precision slit was introduced in the apparatus. The precision slit placed at 40 meters from the X-Ray source, is used as a secondary source in order to focus the beam to an horizontal angular distribution low enough for being accepted by the nano-focusing optics. Nevertheless, after the completion of the EBS project, the source size is

strongly reduced, lessening the need of a further collimation on the horizontal direction of the beam, making questionable the need of the precision slit. However, the additional benefits of using the precision slit, such as the screening of the primary source, which leads to a reduction of the overheating of the downstream optics, and the improvement of the stabilization of the focal spot, make the precision slit still useful in the optics hutch.

The last components discussed in the present section are the Si and Ge filters. These filters can be added or removed from the beam path providing the possiblity to reduce or increase the beam intensity. Whenever the filters are introduced, they absorb part of the beam, thus reducing the intensity impinging on the sample. A reduction of the beam intensity might be required for thicker samples that produce a strong XRF signal. Indeed, in this situation the signal measured by the XRF detectors can saturate. This would avoid the possibility to get any information from the XRF maps obtained since all the pixels would provide the same value, being saturate.

2.2.2. Experimental Hutch

The experimental hutch represents the end-station of the whole apparatus which accommodate different elements such as the nano focusing optics, the sample stage, the microscope, and different detectors, offering a variety analytical techniques at nano-scale: XRF, XAS, XEOL, XRD and 2D/3D phase contrast imaging. An overview of elements present in the experimental hutch is reported in Figure 2.4.
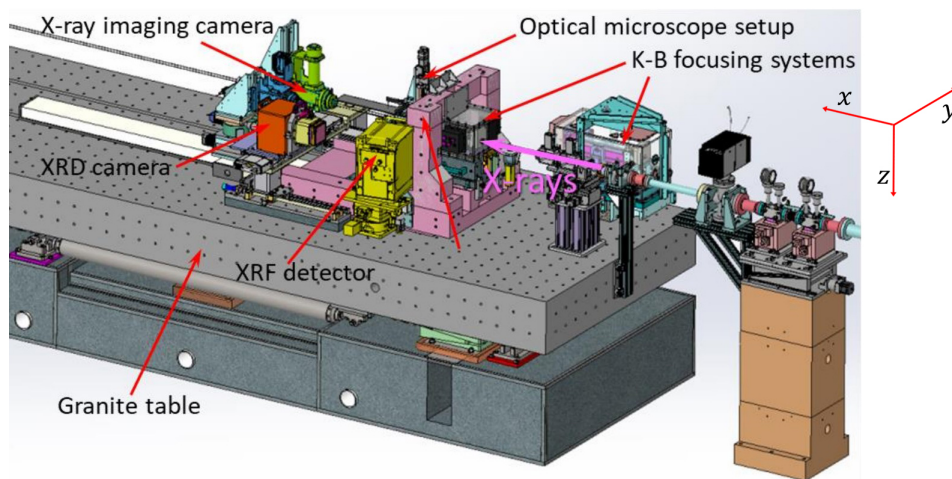

Figure 2.4: Schematic representation of the elements present in the experimental hutch of ID16B [40].

All the instruments present in the experimental hutch are supported by a granite table

$(4.4m \cdot 1.5m \cdot 0.3m)$ which reduces amplification of vibrations present at the level of the floor and allows to eliminate relative vibration between different elements of the apparatus. The granite table is characterized by one degree of freedom along the z vertical direction, in order to adapt the height of the instruments to the different modes of operations, namely the pink mode and the monochromatic mode, introduced in subsection 2.2.1.

The first elements of the experimental hutch is the Kirkpatrick–Baez (KB) mirror system, which allows to focus the X-ray beam from a few microns down to a nano-scale beam spot-size. More specifically, the KB system is composed by two different devices, each one adapted to a specific energy range of the X-ray beam. A dynamically bent multilayer KB system is used for focusing the beam in the energy range between 17 keV and 34 keV, while a fixed curvature grazing incidence KB system is used in the range between 4 keV and 14 keV.

In Figure 2.5 the Full Width at Half Maximum ($FWHM$) of the beam spot size in the horizontal and vertical direction for the two KB systems is shown depending on the second source geometry (the precision slit) chosen. As can be seen, the highest focusing along horizontal direction is achieved fixing the secondary source aperture, namely the precision slit, at 20 μm, at the expense of a reduction of the flux. Contrarily, the vertical beam spot-size is not influenced by the second source geometry which is designed for a horizontal focusing only, as explained in subsection 2.2.1. Thus, fixing the second source aperture to 20 μm would provide a horizontal beam spot-size smaller with respect to the vertical direction, making the beam spot asymmetric. The horizontal precision slit aperture is then set to 50 μm. As can be noticed from Figure 2.5, the highest focusing is achieved in the high energies. Moreover, it's important to notice an energy gap between 14 keV and 17 keV where none of the two KB allow to focus the beam, making this range not operational.

The samples stage mounted on the granite table is composed of different parts: a translation stage along the three x, y and z directions and a rotation stage.
As can be noticed from Figure 2.4 the x direction coincide with the incoming beam direction. Translations along this direction are made possible by the use of air pads which work with pressurized air along a guide over 300 mm. The use of air pads allows high precision adjustment of the sample position. Adjusting sample position along this direction allows either to place the sample in the focal plane of the focused beam or to place the sample at specific distances for phase-contrast imaging analysis. It's important to stress that the beam is considered focused on a distance of ≈ 50 μm along the x direction, thus requiring the sample to be characterized by a maximum thickness of 50 μm for XRF
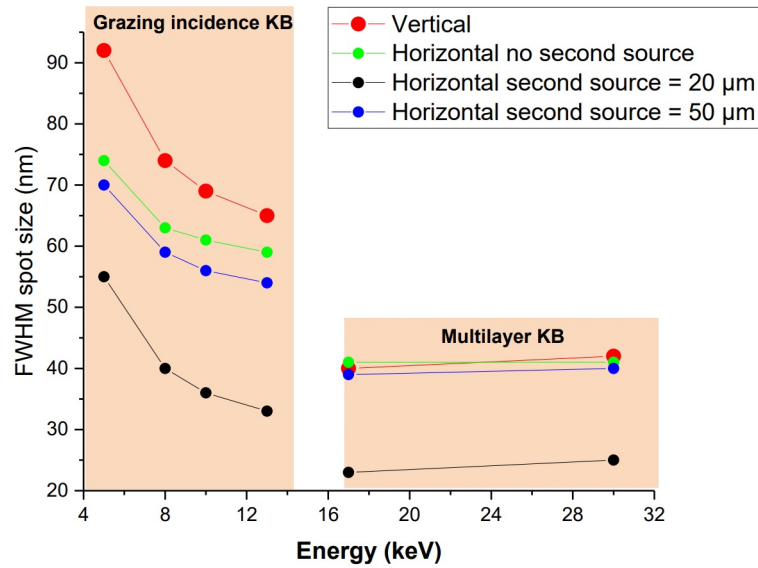
Figure 2.5: FWHM of the beam spot size along horizontal and vertical direction depending on the geometry of the second source aperture chosen [40]

analysis. Indeed, a thicker samples would possibly provide artefacts, as shown by different tests performed at ID16B. Whenever the required position is achieved along x direction, the pressurized air is stopped to increase the stability. Differently from x direction, translations along both y and z work with two different types of motors. Two stepper motors allow fast but low precision translations along these directions. An additional piezostage mounted on the sample stage offers two additional piezomotors characterized by minimum steps of 30 and 40 nm, respectively, thus providing high precision adjustments of the sample position. All these adjustments along different directions can be performed remotely by means of a software, which allows to impart remote controls from the beam line work station. The rotation stage mounted on top of the translation stage allows phase-contrast imaging experiments, where the sample constantly rotate during the acquisition.

In concomitance of the sample stage, the presence of a Visible Light Microscope (*VLM*) provides support to the user to correctly position the sample before the analysis. In particular, the focal plane of the VLM is aligned with the focal plane of the X-ray beam, thus allowing a simple positioning along the x direction of the sample. Moreover, the VLM helps the user during the initial procedure, when the region of interests on the sample are selected.

The experimental hutch is also equipped with several photo diodes placed in different positions along the x direction, providing the possibility to record the incoming X-ray

beam intensity and track its position. In particular, the photo diode placed in concomitance of the VLM microscope allows to record the beam flux at the sample position, providing the possibility to check the correct intensity expected for the flux. Additionally, recording the beam flux during XRF measurements allows further quantification of the chemical composition of the sample, as explained in subsection 2.3.3.

Concerning the different detectors present in the experimental hutch, only those used in the present study will be presented in subsection 2.2.3, thus the ones needed for XRF technique and 3D phase contrast imaging.

2.2.3. Detectors for XRF and nano-tomography

Two devices comprehending a total of 10 Silicon Drift Diode (SDD) detectors are available for XRF analysis as reported in Table 2.2, allowing to analyze samples from different directions, with a typical energy resolution of ≈ 150 eV. This is considered low enough to resolve the emission lines of different chemical elements.
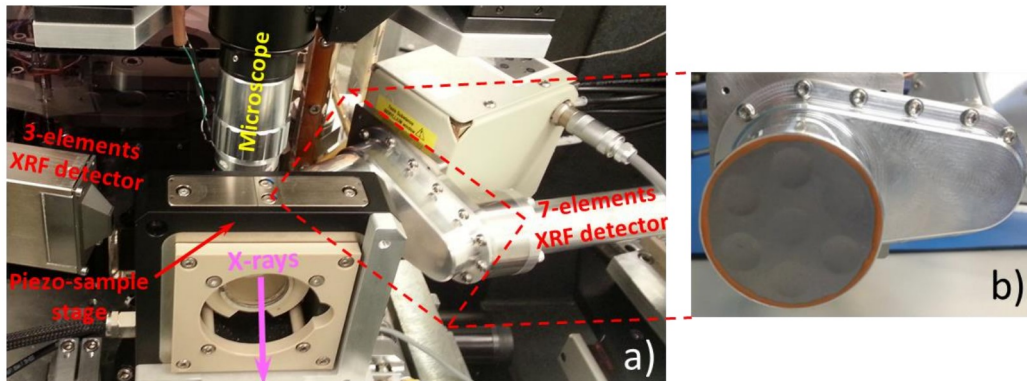

Figure 2.6: (a) Overview on the two main XRF detectors, the piezoelectric sample stage and the VLM present in the experimental hutch [40]. (b) Zoom on the 7 SDDs composing the MIRION fluorescence detector

The first XRF detector is shown on the right side of Figure 2.6.a. It is a seven-elements detector, as shown in Figure 2.6.b, from MIRION Technologies (Canberra BNLS) NV placed at ≈ 35 mm from the sample, characterized by a hexagonal close-packed geometry, with 50 mm^2 area for each detector, a Silicon thickness of 0.5 mm and a Be window, equipped with a CUBE pre-amplifier technology. A second device, shown on left side of Table 2.2.a, comprehend three SDD detectors with same specification of the previous one, placed at 30 mm from the sample. Space constraints made necessary to have two different devices. Indeed, on one side of the sample stage there is less available space with respect to the other side. Both devices are placed at $\approx 75°$ with respect to the X-ray

beam propagation direction, with the aim of minimizing the scattering, even though the ideal angle would have been of 90°, but not feasible again due to spatial constraints.

Product	n of detectors	Si thickness	Active area
MIRION Technologies	7	0.5 mm	50 mm^2
Hitachi ME3	3	0.5 mm	50 mm^2

Table 2.2: Detectors used at ID16B for XRF analysis. The active area is to be considered for each SDD detector

The setup used for nano 3D phase-contrast imaging acquisition is composed by three main elements: a thin scintillator crystal, a visible-light optics system and a digital camera, as shown in Figure 2.7. A thin scintillator crystal receive the X-ray radiation transmitted through the sample and generate a luminescence image, then projected magnified by the visible-light optics onto a digital camera. The digital camera used is based on CMOS techology and is characterized by a 2560·2160 pixel grid and a 16 bit dynamic range. The acquisition procedure for holotomography requires to record different images of the sample, as better explained in section 2.4.
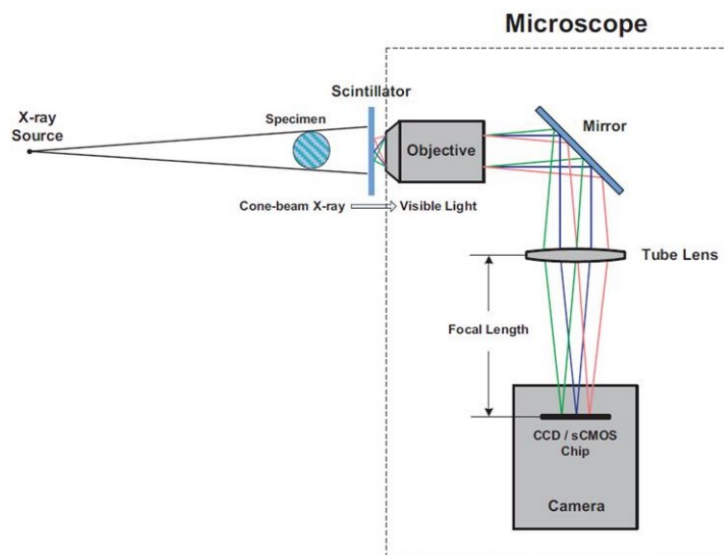

Figure 2.7: Schematic representation of the phase-contrast imaging acquisition system.

2.3.   NanoXRF at ID16B

XRF technique technique allows to determine the chemical composition of the samples by analyzing the fluorescence radiation emitted. In particular, synchrotron radiation source, together with the complex experimental apparatus introduced in section 2.2, allows to achieve a nano-scale spatial resolution.

2.3.1.   The theory behind XRF technique

In Figure 2.8 is depicted a simplified representation concerning the processes involved in generation of fluorescence radiation, with the aim of better clarifying the physics behind XRF technique explained in the following.
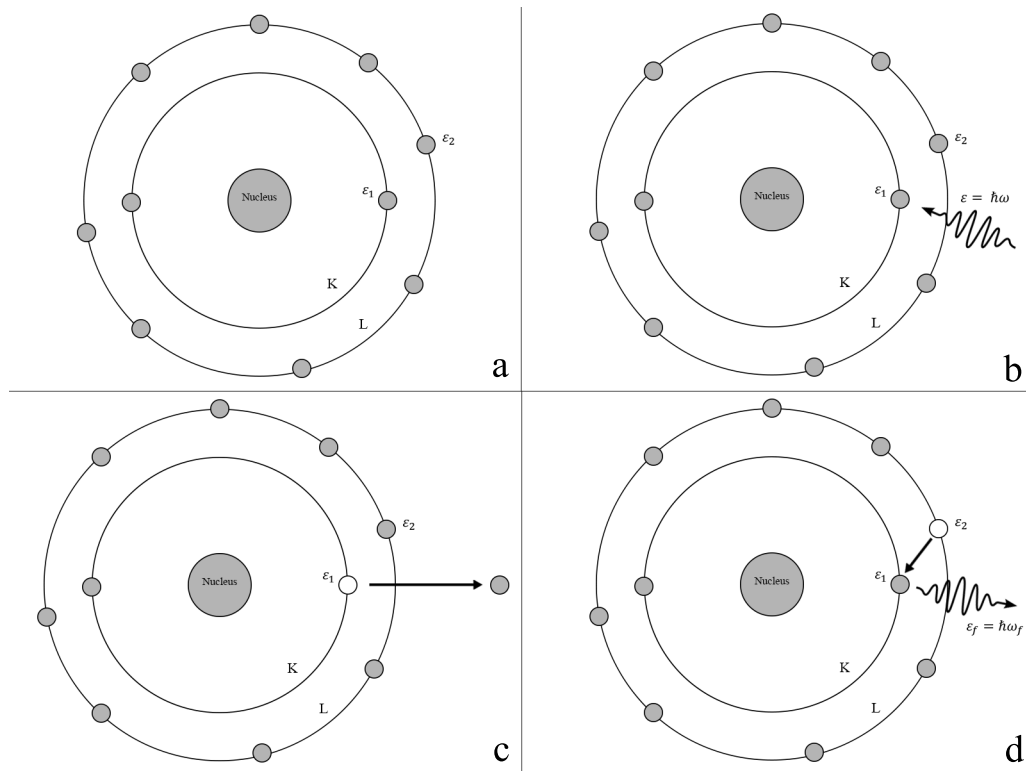

Figure 2.8: Simplified representation of the working principle of XRF. (a) Atomic structure with electrons represented by circles. Electronic shells are label with capital letters. (b) Incoming X-ray photon ε interact with an electron. (c) The photo emission process produce a vacancy in the electronic structure. (d) The atom relaxes toward a stable state emitting fluorescence radiation with energy $\varepsilon_f = \varepsilon_2 - \varepsilon_1$.

Since the introduction of Rutherford-Bohr's model for the atomic structure in 1913, we consider electrons occupying stationary states around the atomic nucleus as bounded

electrons, as a result of the attractive electrostatic interaction experienced due to the presence of the positively charged atomic nucleus. Each of those stationary state is characterized by a binding energy ε_i[1] (Figure 2.8.a). Providing an amount of energy ε to a bounded electron characterized by a binding energy ε_1 such that $\varepsilon > |\varepsilon_1|$, allows to excite the electron to an unbounded state becoming then a free electron; a phenomenon called photoelectric effect. In XRF technique a source of X-rays with energy $\varepsilon = \hbar\omega$ is focused on a sample, leading to emission of electrons from the atoms composing the sample (Figure 2.8.b). The emission of an electron from an atom creates a vacancy in the electronic structure (Figure 2.8.c) ,i.e., a non-occupied electronic state, which makes the overall system unstable. Consequently, the atom undergoes to a relaxation process to evolve back to a stable state. In the specific case of XRF, the relevant relaxation process is fluorescence, which consists in a first de-excitation event where a bounded electron occupying a higher energy state ε_2 (i.e., $\varepsilon_1 < \varepsilon_2$) relaxes into the unoccupied state ε_1. This process leads to the emission of a photon (or fluorescence radiation) by the atom (Figure 2.8.d), whose energy ε_f can be easily retrieved by an energy balance:

$$\varepsilon_f = \hbar\omega_f = \varepsilon_2 - \varepsilon_1 \tag{2.1}$$

Considering that each atomic species have a unique set of binding energies ε_i for the electronic states and noticing that the fluorescence radiation energy ε_f depends on the difference between these binding energies (Equation 2.1), it's simple to conclude that each atomic species is characterized by a unique set of values for the energy of the fluorescence radiation emitted ε_f.

The energy-dispersive XRF spectrum obtained from a direct measurements on a sample present different peaks, each one associated to photons characterized by different energies ε_f. Each of those peaks is associated to a fluorescence relaxation process occurred in different atomic species. Knowing the characteristic radiation energies ε_f emitted by different chemical elements provides the possibility to interpret the spectra obtained, identifying the peaks and thus the chemical composition of the sample.

As previously mentioned, the relaxation process involves a de-excitation event where a bounded electron occupying a higher energy state relaxes into a lower energy vacancy. Vacancies can be formed in different electronic states and the de-excitation event can occur from different higher energy electronic states. Depending on the combination of the states involved in the process, different labels are used to identify the fluorescence radiation generated, typically relying on the Siegbahn notation [44]. The energy level of the vacancy

---

[1]Considered here as a negative quantity $\varepsilon_i < 0$

determine the first capital letter associated to the transition (e.g., K, L, M and so on). The energy level of the electrons which undergoes to de-excitation defines the second greek letter (e.g., α_1, α_2, β_1 β_2 and so on). The peaks observed in XRF spectra provide also information regarding the concentration of the chemical elements. Indeed, the intensity of these peaks varies depending on the concentration of the chemical element associated to each peak. Higher concentration of a specific element in the sample will produce more fluorescence photons, resulting in a higher intensity peak. Contrarily, elements present in low concentration will produce a smaller number of fluorescence photons, resulting in lower intensity peaks. Nevertheless, an initial calibration procedure is typically needed before quantification, as described in subsection 2.3.3.

2.3.2.   Practical issues in XRF technique

Interpreting the data from XRF measurements is less straightforward than what might appear considering the simple theory at the basis of this technique. The presence of different chemical elements within the samples provide a heterogeneous XRF spectrum characterized by different fluorescence peaks. In several cases the composition of the sample is known a priori, for instance, as reported in a study on electrolysis cells by Villanova et al. [45]. This provide a more simple interpretation of the XRF spectra obtained. In other cases, as it is for the present study, the chemical composition of the sample is not completely known a priori, and it's usually heterogeneous in the specific case of organic samples as shells. Moreover, additional peaks can be present in the spectrum, associated to components present in the experimental hutch. In particular, the composition of the detectors, the presence of air and possible additional impurities must be properly accounted when XRF data are analyzed. Scattering phenomena, pile-up effects and escape peaks introduce additional features in the spectrum which must be accounted as well.
The use of specific software for XRF data analysis helps the user to determine and quantify the composition of the sample probed, usually through a process of trial and error, with the aim of refining the fitting of the data. These software are usually capable of accounting for all the additional peaks that might be present as consequence of the different phenomena just described. Moreover, different parameters concerning the experimental setup, the sample main composition, etc., can be considered using these software in order to refine the results.

2.3.3.   Software for XRF data analysis

In the present study PyMca software [46] was employed to analyze the measured spectra. The first step for analyzing spectra required a normalization procedure, to take

into account the cyclic fluctuations of the incoming X-ray beam flux over time, associated to the electron beam fluctuations in the storage ring [2]. The normalization procedure exploited a photo diode placed at the sample position, previously introduced in subsection 2.2.2, which allowed to record the X-ray signal considered as a background signal, then subtracted to the XRF signal. A calibration procedure was also required for defining a correspondence between the channels of the SDD detector and energy scale, relying on emission peaks of elements whose presence was known. In the present analysis, Ca and Sr were used for calibration since these elements are known to be present in the shell structure, as introduced in section 1.1. Moreover, the presence of Mo inside the XRF detector assured the recurrence of the Mo K-line in the spectrum. Finally, the elastic scattering peak was included for calibration since the beam energy is known with high resolution. An example of a normalized and calibrated spectrum obtained from nano-XRF performed on one of the samples is reported in Figure 2.9
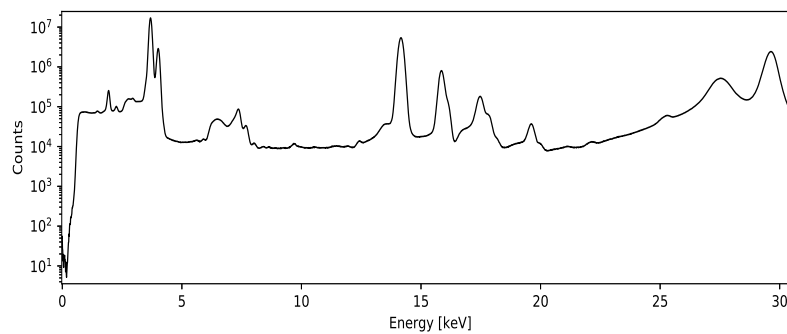

Figure 2.9: Example of a normalized spectrum from map $n°2$ of sample G0 after calibration.

The fitting procedure was performed with PyMca which allowed to set a wide range of adjustable parameters to further refine the results:

- Set the beam energy. This parameter was fundamental for the fitting process. Indeed, closer the emission line of an element is to the beam energy, stronger the intensity of the associated peak is expected to be. This effect needs to be properly accounted from the software.

- Define the expected peak shape by setting the peaks' tail area and slope. This allowed to manually adjust the fitting, so that it better fitted the raw spectrum.

- Define the thickness and composition of attenuators, such as the air between the

---

[2]The electron beam in the storage ring loses electrons over time, resulting in a decrease of the X-ray flux generated. Every ≈ 1 hour electrons are injected in the storage ring to restore the intensity of the electron beam, giving rise to a cyclic fluctuation of the X-ray flux.

sample and the camera, the window of the detector and the matrix composing the sample. These parameters are fundamental during the quantification process. Indeed, presence of attenuators such as the air between the sample and the detector lead to attenuation of the fluorescence radiation measured. Same principle works for the detector window and the matrix composing the sample. Thus, PyMca takes into account the attenuation of the radiation due to the presence of these mediums between the sample and the detector.

- Set the incident angle on the sample and the outgoing angle depending on the position of the detector. This parameter was fundamental to properly account for inelastic Compton scattering. Indeed, this effect depends on the angle between the direction of the incoming beam and the direction at which the radiation was collected.

- Define the offset of the detector and the detector noise.

PyMca allows to take into account the presence of additional peaks associate to scattering effects, distinguishing between the elastic scattering peak and the inelastic Compton scattering peak. Another features provide the possibility to consider pile-up effects, usually observed in presence of a sample with high concentration of an element (Ca in the present case), giving rise to additional peaks in the spectrum. The fitting procedure allowed to identify the fluorescence peaks observed in Figure 2.9, obtaining Figure 2.10, further discussed in section 4.1.
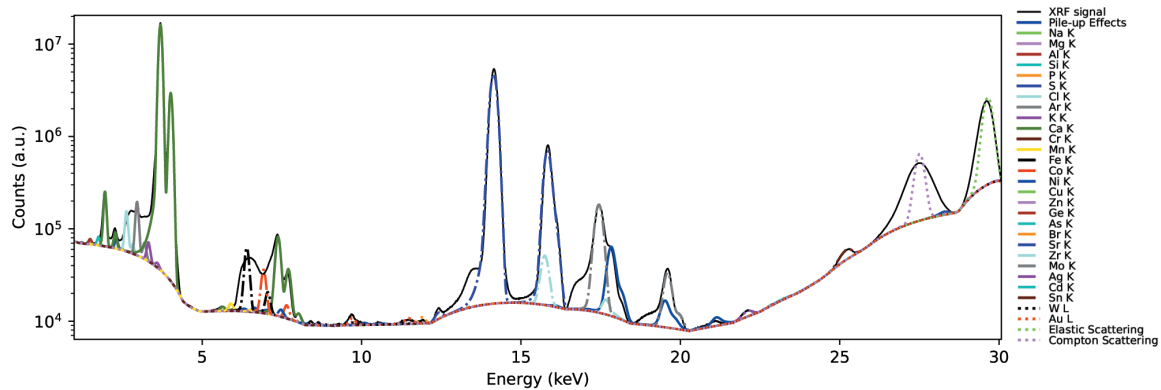

Figure 2.10: Results from fitting of the spectrum reported in Figure 2.9

Once the fitting procedure is over, PyMca allows to perform quantification of the chemical composition by setting some fundamental parameters (photon flux, total exposure time, active area of the detector and detector-sample distance) providing a fast procedure for quantification. Nevertheless, not all the fundamental parameters are usually known precisely, thus, an alternative procedure consider a first step where a reference

sample (presented in subsection 2.3.4) of known composition is probed. This measurement allows to calibrate the emission peaks observed in the reference sample spectra, by associating at each peak the known concentration of the correspondent element. This additional step allows to recover the missing fundamental parameters, which can then be set for quantification of the samples analyzed.

Further analysis of the results were performed importing data in MATLAB software [47].

2.3.4. Reference sample for quantification

A reference sample with known composition allows to calibrate the intensities of the emission peaks in XRF spectra as introduced in subsection 2.3.3. In the present study, the reference sample considered for calibration is AXO C10 provided by Anton Paar [48] composed by a $5 \cdot 5mm^2$ frame in which a $2 \cdot 2mm^2$ membrane $200nm$ thick of Si_3N_4 is present. The thin membrane is coated with Titanium, Cromium, Iron and Copper in known quantities, as reported in Table 2.3.

Element	Mass deposition $[ng/mm^2]$	Emission lines (K_α) [eV]
Cu	23.7 ± 1.3	8040
Fe	31.3 ± 1.4	6041
Cr	65.6 ± 3.5	5412
Ti	54.5 ± 7.4	4510

Table 2.3: Coating elements of the reference sample AXO C10.

An XRF map of $20 \cdot 20 \ \mu m^2$ with resolution of $0.2 \cdot 0.2 \ \mu m^2$ and $100 \ ms$ exposure time (per pixel) on AXO C10 reference sample was performed for calibration of emission peaks for further quantification. The beam energy, beam spot-size and other parameters are the same used during the samples analysis, reported in subsection 2.3.5. Only the data acquired with one SDD detector (the central one showed in Figure 2.6.b) from the MIRION Technologies device were considered for calibration, since different detectors provided the same parameters for the calibration.

2.3.5. Preliminary settings for nano-XRF analysis

The X-ray beam energy was set to 29.6 keV in pink beam mode characterized by an energy resolution of $\Delta E/E \approx 10^{-2}$, small enough to resolve the emission peaks of different elements. A calibration procedure allowed to properly adjust the nano-focusing optics to achieve a beam spot-size of $60 \cdot 64 \ nm^2$. Moreover, five filters of both Ge and Si were

introduced with a total thickness of Ge of 400 μm and 1.5 mm of Si, achieving a photon flux intensity at the sample position of $I \approx 9.77 \cdot 10^{10}$ ph/s.

2.4.   Nano-scale tomography at ID16B

Nano-tomography technique provides information about the 3D mass density distribution within the sample volume, being sensitive to both heavy and light elements.

2.4.1.   The theory behind tomography imaging

An X-ray beam passing through an object can experience two possible effects, both attenuation and phase shift, depending on the object composition. More specifically, these two phenomena depend on the complex refractive index which characterize the object, that can be expressed as:

$$n = 1 - \delta + i\beta \tag{2.2}$$

The real part corresponds to the refractive index $(1 - \delta)$ and it's associated to phase shift effects, while the imaginary part (β) is associated to the absorptive properties of the sample.

To better clarify the phase shift effect together with absorption, and how these phenomena allow to retrieve teh 3D mass density distribution withing the sample, let's start considering an X-ray field. The scalar complex wave function Ψ describes the X-ray field, representing one of the component of the electromagnetic field (i.e., one among E_x, E_y, E_z, B_x, B_y or B_z) and thus satisfying the free space d'Alembert equation:

$$\left(\frac{1}{c^2}\frac{\partial^2}{\partial t^2} - \nabla^2\right)\Psi(x,y,z,t) = 0 \tag{2.3}$$

where ∇^2 represents the three dimensional Laplace operator.

The X-ray field, being a complex function, can be expressed as a product between the intensity of the field and a phase term:

$$\Psi(x,y,z,t) = \sqrt{I(x,y,z,t)}e^{i\phi(x,y,z,t)} \tag{2.4}$$

where I represents the intensity of the field and is related to the scalar X-ray field as:

$$I(x, y, z, t) = |\Psi(x, y, z, t)|^2 \tag{2.5}$$

while ϕ represents the phase of the wave. It's important to highlight that the intensity of the field is the quantity that is experimentally measured, rather than the X-ray field Ψ.

Absorption and phase shift effects

Let's now assume that the X-ray field Ψ propagates along the z direction, considered as the optic axis. This field propagates through an object totally contained within the portion of space $0 \leq z \leq z_0$, as shown in Figure 2.11.
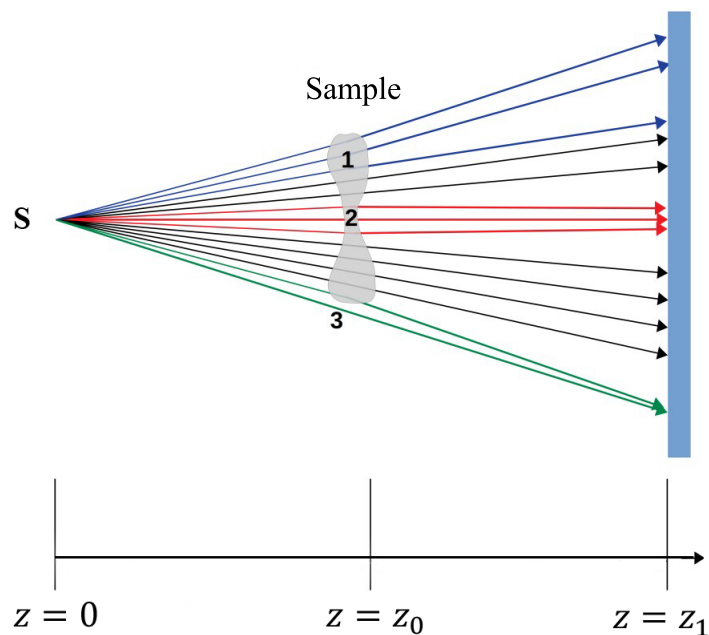

Figure 2.11: Schematic representation of a tomography imaging system. S represent the source of the X-ray beam which is focus on a sample. The exiting surface of the sample corresponds to the plane $z = z_0$. Different regions within the sample, such as a local low density region (**1**), a local high density region (**2**) and an edge region (**3**), produce a varying transverse intensity distribution $I(x, y, z = z_1)$, providing the base to propagation-based phase-contrast imaging.

Following the discussion proposed by Paganin [49], and introducing suitable assumptions, it can be shown that the wave field of the X-ray beam at the exit surface of the sample $\Psi(x, y, z = z_0)$ where a position-sensitive detector is placed, is related to the wave

field at the entrance surface $\Psi(x, y, z = 0)$ by a factor T, defined as the transmittance function:

$$\Psi(x, y, z = z_0) = \Psi(x, y, z = 0) \cdot T(x, y) \tag{2.6}$$

$$T(x, y) = exp\left\{-ik \int_{z=0}^{z=z_0} [\delta(x, y, z) - i\beta(x, y, z)]dz\right\} \tag{2.7}$$

where k represents the wave number of the field. As can be noticed from Equation 2.7, the wave field, after propagation through the object, encodes the information regarding the complex refractive index. The relation between the two fields can also be expressed in terms of the intensity of the fields taking the squared modulus of Equation 2.6, giving:

$$I(x, y, z = z_0) = I(x, y, z = 0)e^{-\int_{z=0}^{z=z_0} \mu(x,y,z)dz} \tag{2.8}$$

This equation is known as Beer-Lambert law and accounts for the attenuation of the electromagnetic radiation that propagates through a sample characterized by a linear attenuation coefficient μ. The connection between the imaginary part of the complex refractive index (β) and the X-ray attenuation previously mentioned, is straightforward considering the linear attenuation coefficient defined as :

$$\mu(x, y, z) = 2k\beta(x, y, z) \tag{2.9}$$

As can be noticed, there's no dependence on the real part of the complex refractive index (δ) in Equation 2.8, while the dependence from β is preserved from Equation 2.6 to Equation 2.8.

Beer-Lambert law provides the basis for absorption contrast imaging technique. Indeed, the resulting image obtained at the exit surface contains information regarding the sample. In particular, knowing both $I(x, y, z = 0)$ and $I(x, y, z = z_0)$ allows to retrieve the projected linear attenuation coefficient $\int \mu(x, y, z)dz$ characterizing the object and related to absorption effects.

An important assumption introduced by Paganing et al. [49] to obtain Equation 2.7 and Equation 2.8 is the so called *projection approximation*, which allows to express the attenuation (and the phase shift $\Delta\phi$ introduced in the following) as line integral. This approximation requires the sample to be slowly varying (or considered thin) compared to the resolution of the acquisition system. In high-resolution X-ray analysis the sample thickness become large compared to the resolution, thus undermining the validity of this approximation.

An additional effect associated to the propagation of the wave field through the object is to accumulate a phase shift at the exit surface of the object, obtainable from:

$$\Delta\phi(x,y) = -k \int \delta(x,y,z)dz \qquad (2.10)$$

As can be noticed, the phase shift is associated to the real part of the complex refractive index (δ). Nevertheless, no observable effects associated to the phase shift are shown in Equation 2.8. More information about the object can be extracted from the X-ray field if the effects produced by the phase-shift could be detected, especially in weakly absorbing samples (e.g., soft tissues) where absorption contrast imaging provides poor information.

A suitable solution considers an alternative setup where the detector, rather being positioned at the exit surface plane of the object $z = z_0$, is instead placed in the plane $z = z_1$, as shown in the simplified representation of Figure 2.11. In this case, the propagation of the exiting field after the object provide observable effects associated to the phase-shift occurred during propagation through the object. More specifically, the transverse X-ray phase shift $\Delta\phi(x,y)$ at the exit surface of the object, produces an observable transverse intensity distribution $I(x,y,z=z_1)$, recorded by a position-sensitive camera. This technique is named propagation-based phase-contrast imaging.

The inverse problem for 2D phase-map retrieval

The first step after recording a single-distance phase-contrast image (i.e., the intensity $I(x,y,z=z_1)$, by means of a position sensitive detector) is to retrieve the 2D phase map $\phi(x,y)$ associated to the X-ray beam at the exiting surface of the sample. Following the discussion proposed by Paganing et al. [49], the phase map retrieval is made possible by solving an inverse problem. Paganin et al. [49] proposed a phase-retrieval formula derived as a solution of the transport of intensity equation, assuming projection approximation to be valid. This equation provides the missing phase $\phi(x,y)$ (2D phase-map) which contains information about the projected complex refractive index of the sample, once $I(x,y,z=z_1)$ is measured by a position sensitive detector.

Reconstruction algorithm from multiple 2D phase-maps

Tomography analysis require to measure several images of the sample over different angles. For this purpose, the position-sensitive cameras acquire images while the sample is set into rotation over 360°. In this way, different 2D phase maps are obtained from different

angular positions of the sample. Subsequently, a iterative reconstruction algorithm is exploited to combine the different 2D phase-maps and finally retrieve the final 3D mass density distribution of the sample.

In the present study a iterative algorithm based on alternating projections was employed for the reconstruction procedure.

In addition, by measuring images at different sample-focal plane distances, a better phase contrast across all spatial frequencies could be obtained, thus reducing the effects of noise and achieving an improved spatial resolution [50]. This techniques is known as holographic tomography, and it was employed in the present study.

2.4.2. Software for nano-tomogrpahy analysis

The data obtained from the reconstruction process, briefly discussed in subsection 2.4.1 were examined with the help of ImageJ software [51]. This software provides different features suitable for imagining studies. The main feature utilized for examining the different regions of the shells, looking for changes in density within the shell structure, was the *Threshold* function. It allows to add a red overlay to the image specifying the range of intensities included, as shown in Figure 2.12, easily moving through the stack of images. In this way, it was checked the presence and the location of both higher density and less dense regions within the shell structure. Additionally, a segmentation procedure was performed relying on *3D Analysis* plugin available for ImageJ software.

MATLAB software [47] was exploited relying on the *volumeViewer* function [52] to generate the 3D rendering from the stack of images. One of the features provided by this function is to set thresholds to differentiate regions characterized by different densities to better distinguish them in the 3D rendering.

2.4.3. Preliminary settings for nano-tomography analysis

An alignment procedure allowed to set the X-ray beam energy to 29.6 keV in pink beam mode, achieving a $\approx 70 \cdot 70 \ nm^2$ beams spot-size. Different filters of Si were added, achieving a total thickness of 1.5 mm to reduce the beam flux avoiding saturation of the camera.
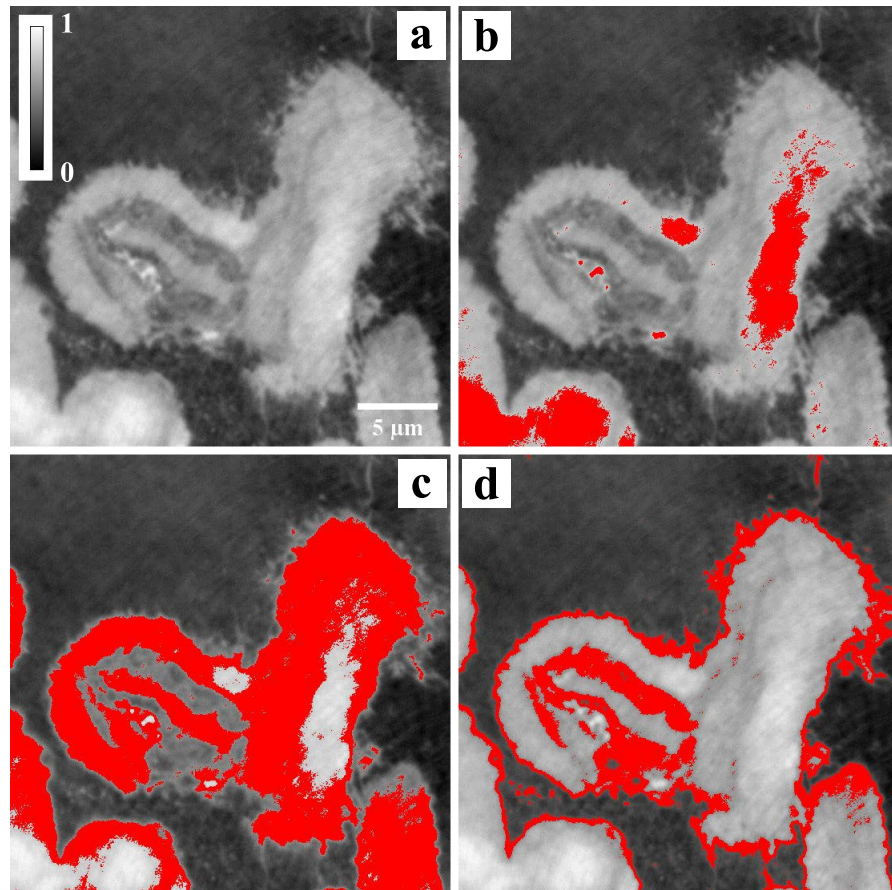
Figure 2.12: Example of a gray-scale 16-bit image showing a slice inside the periostracum region from a 50 nm holo-tomography measurement. The intensities were normalized to the maximum value. (a) shows a cavity region in grey scale. Higher intensity corresponds to low density regions and low intensity for higher density regions. (b) shows a red overlay including intensities from 0.80 to 1.00 representing less dense regions. (c) shows a red overlay including intensities from 0.65 to 0.80 representing denser regions. (d) shows a red overlay including intensities from 0.50 to 0.65 representing even denser regions. All intensities below 0.50 value were assumed to be associated to the $CaCO_3$ matrix. Thresholds were set utilizing the *Threshold* function provided by ImageJ software.

3 | Sample preparation

The present chapter describes the procedure followed for preparing samples for the different experimental techniques exploited. In section 3.1 will be presented the procedure followed for preparing samples for nano-XRF analysis, while section 3.2 describes the procedure for nano-tomography sample preparation.

3.1. Samples for nano-XRF technique

Three samples of *Patella caerulea*[1] were prepared before being analyzed with nano-XRF technique. In particular, two samples were collected from the polluted area of Gabes, and one sample was collected from the less polluted area of Zarat, as previously introduced in section 1.7. The region analyzed was the apex of the shell for all the samples, since this region includes both the oldest part of the shell in the outer layer and the newly formed part in the inner layer, thus keeping track of possible environmental stress over the whole life of the mollusk.

The samples were initially cleaned separately in ultrasonic bath with ethanol for 8 minutes in order to remove possible impurities present on the surfaces. Subsequently, a precision cutting machine (*Accutom-100*, Struers) was used to perform a first cut on the samples (Figure 3.1.a), with the aim of dividing the samples in two parts revealing the cross section of the shell (Figure 3.1.b). An additional cut was performed in the perpendicular direction to reduce the size of the sample, as shown in Figure 3.1.b, where the right side tip region is lacking. During the cutting procedure a clamping tool was utilized for fixing the sample to the cutting machine. The additional use of some tissue paper placed between the contact points of the shell and the clamping tool prevent fractures when the clamp was tightened. All parameters for the cutting procedure can be found in Table 3.1.

---

[1]Samples were provided by our collaborator Youssef Lahbib, Université de Carthage, Faculté des Sciences de Bizerte
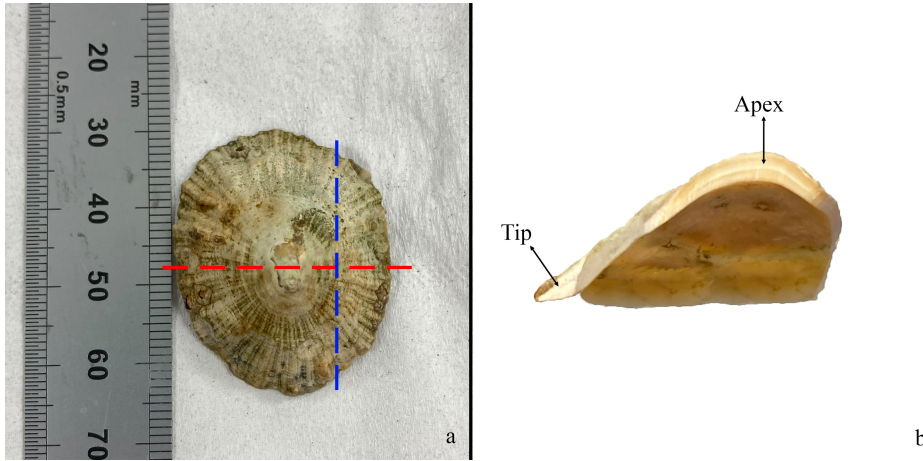
Figure 3.1: (a) Top view of the seashell. The red dotted line represents the direction followed during the first cut. The blue dotted line represents an additional cut to reduce size of the sample (b) Photo of the shell cross section exposed to view after the first two cuts.

Struers *Accutom-100* settings	
Blade	40A15
Blade speed	3000 rpm
Feed speed	0.080 mm/s
Length of cut	> 10 cm
Cutting force level	Low

Table 3.1: Parameters used for cutting samples with Struers *Accutom-100*. The length of the cut was set higher than the shell diameter to ensure that the sample is completely cut in two parts.

Samples were then embedded in acrylic resin (*LevoCit*, Struers) to facilitate manipulation throughout the subsequent procedure. A second cutting procedure was performed with the cutting machine, obtaining thin disks of resin of thickness $\approx 2 - 3mm$, containing the cross section of the shell, as shown in Figure 3.2. Further transversal cuts were performed with the cutting machine in order to select the region of interest along the cross section (apex) as shown by the red dotted lines in Figure 3.2. As mentioned in section 3.2, nanoXRF technique requires samples to be both thin and characterized by a smooth surface. Hence, considering the limitation of the cutting machine to further reduce the thickness of the samples especially with fragile samples like thin seashell films which could easily break, a different technique is exploited for further reducing sample thickness. A grinding and polishing machine (*TegraForce-1*, Struers) was used, at first for grinding samples, in order to reduce the thickness down to $\approx 50\mu m$ obtaining thin films,

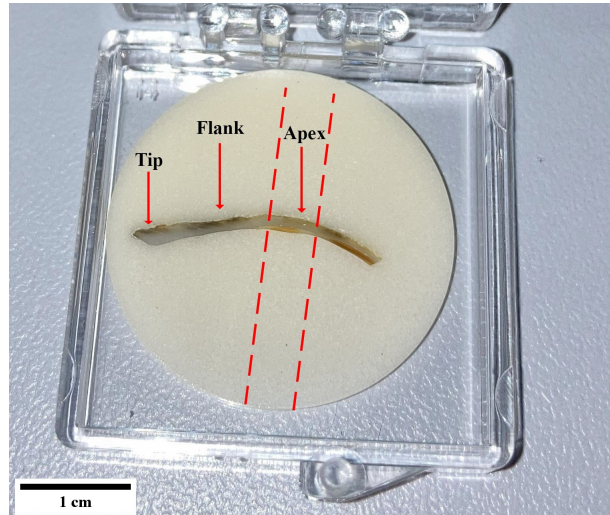and finally for polishing the surfaces of samples.

Figure 3.2: Seashell cross section embedded into acrylic resin and cut into disks. The red dotted lines represent directions followed for additional cut performed to select the region of interest.

The preparation before the grinding procedure, required, at first, to mount the sample reported in Figure 3.2 on the sample mount, fixing it with wax (*Tripod Wax*, Struers), then introducing the sample mount on the tripod device (*TriPod Polishing Fixture*, Struers), which facilitates the manipulation of the sample offering a larger volume to hold during grinding and polishing procedures.

The grinding procedure was performed using SiC foils from Struers with 600 grains size for a quick and rough reduction of the sample thickness, followed by the use of 1200 grain size foils for a more precise thickness reduction. The grinding procedure was conducted with a constant supply of water on the sample and a rotating speed of the machine of 150 rpm. Samples were cleaned with running water once the procedure was over. During the refined grinding procedure with the 1200 SiC foils, the thickness of the samples was routinely checked with the help of a microscope, by comparing the sample thickness with a ruler characterized by 500 μm ticks spacing.

Polishing was performed at first using a polishing cloth (*MD-Mol*, Struers) in synergy with a spray characterized by a diamond suspension of 3 μm size (*DP-Spray P*, Struers), with a rotating speed of 200 rpm for 3 minutes. To further reduce surface roughness, a softer polishing cloth (*MD-Nap*, Struers) was used in synergy with diamond suspensions of 1 μm and 0.25 μm sizes (*DP-Spray P*, Struers) consecutively, again for 3 minutes for both processes.

Once the procedure was terminated, samples were removed from the sample mount by melting the fixing wax with a heating plate machine, and then flipped, in order to polish the other surface [2]. Afterward, samples were removed from the sample mount and another cleaning process with the ultrasonic bath was performed, to remove all the possible impurities introduced during the previous procedures. Finally, samples were removed from the resin with the help of tweezers and mounted on the sample holder for XRF technique, as shown in Figure 3.3. The labelling of the samples defines the location where the sample was collected: G stands for Gabes and Z for Zarat. The number following the letter was added to distinguish samples coming from different shells.
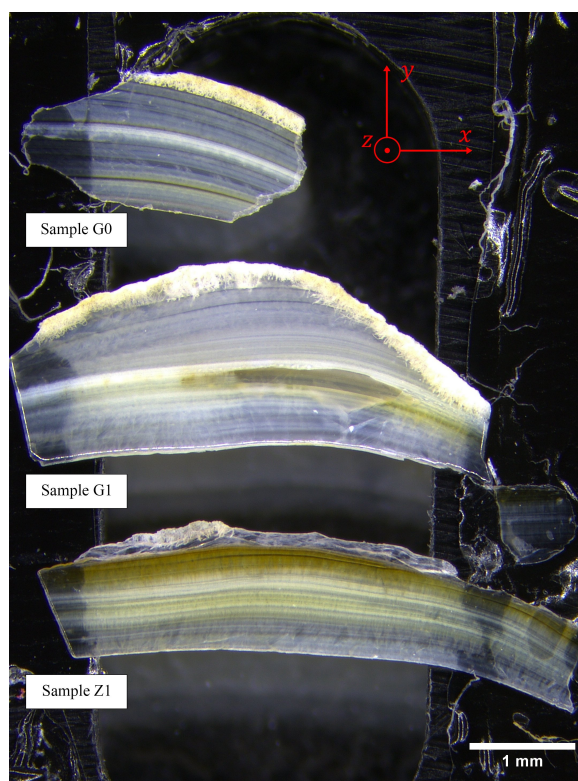

Figure 3.3: Photograph of the three samples prepared for nano-XRF analysis mounted on the sample holder. The labelling of the samples defines the location where the sample was collected: G stands for Gabes and Z for Zarat. The number following the letter was added to identify different samples. The reference axis were added to better understand the orientation of samples reported in Figure 3.7.

---

[2]If needed, the second surface was preliminary smoothed by means of SiC foils with 1200 grain size for ≈ 1 minute, before polishing.

3.1.1. ROI identification for XRF analysis

The criterion chosen for selecting the region of interest on each sample was to probe the shell composition from the outer layer to the inner one, thus over the whole shell width. Due to time constrain this was not possible on sample G1, thus only a section of the shell was probed. Moreover, part of the data concerning sample Z1 were lost during the acquisition as will be better explained in the following. Different XRF maps were performed on the samples rather than acquiring one bigger single map for each sample, in light of the fact that the piezomotors, mentioned in subsection 2.2.2, limit the map dimensions to $100 \cdot 100 \ \mu m^2$. Nevertheless, dividing the XRF acquisition in different maps required a longer acquisition time. The main parameters set for the acquisition are reported in Table 3.2.

Sample	**G0**	**G1**	**Z1**
Pixel size [nm]	200	200	200
Map size [μm^2]	30· 50	20 · 50	30· 50
# of maps	22	17	20
Acquisition time [s]	0.1	0.1	0.1

Table 3.2: Settings for XRF maps for each sample. The acquisition time is inteded per pixel.

Pixel size and acquisition time were set looking for a compromise between spatial resolution and total acquisition time. The regions probed for each of the three samples are reported in Figure 3.4, Figure 3.5 and Figure 3.6 for samples G0, G1 and Z1, respectively. As can be notice, most of the shell width was covered and at least one map per sample was set in order to overlap the outer layer region, the periostracum, to get more insights about possible bioaccumulation, a topic further discussed in section 4.3.
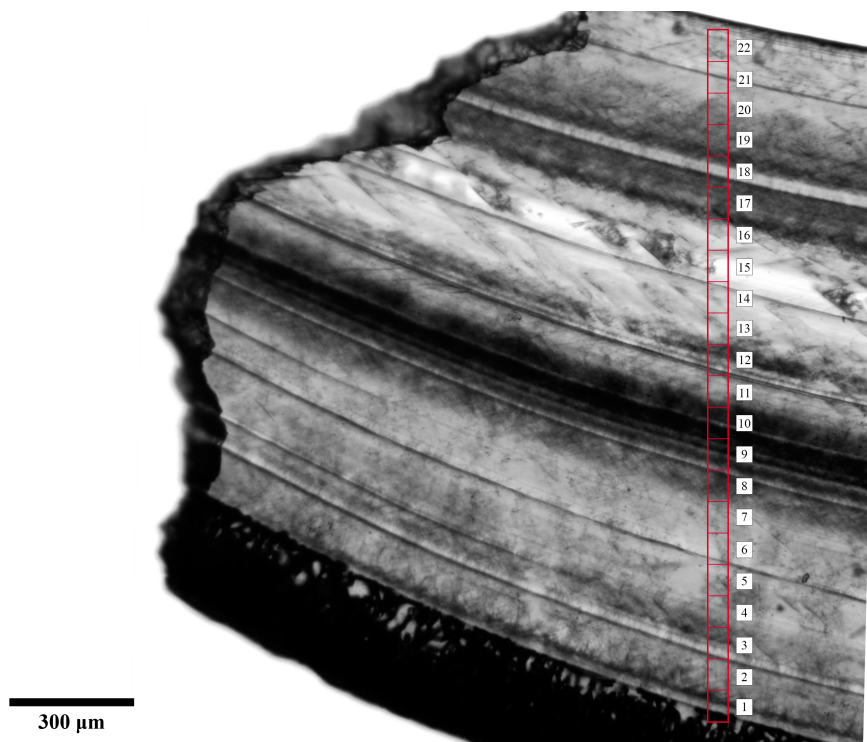
Figure 3.4: Sample G0 visualized with optical microscope 50x enlargement. Red rectangles define the areas analyzed with XRF. Labels identify the different XRF maps.

Figure 3.5: Sample G1 visualized with optical microscope 50x enlargement. Red rectangles define the areas analyzed with XRF. Labels identify the different XRF maps.
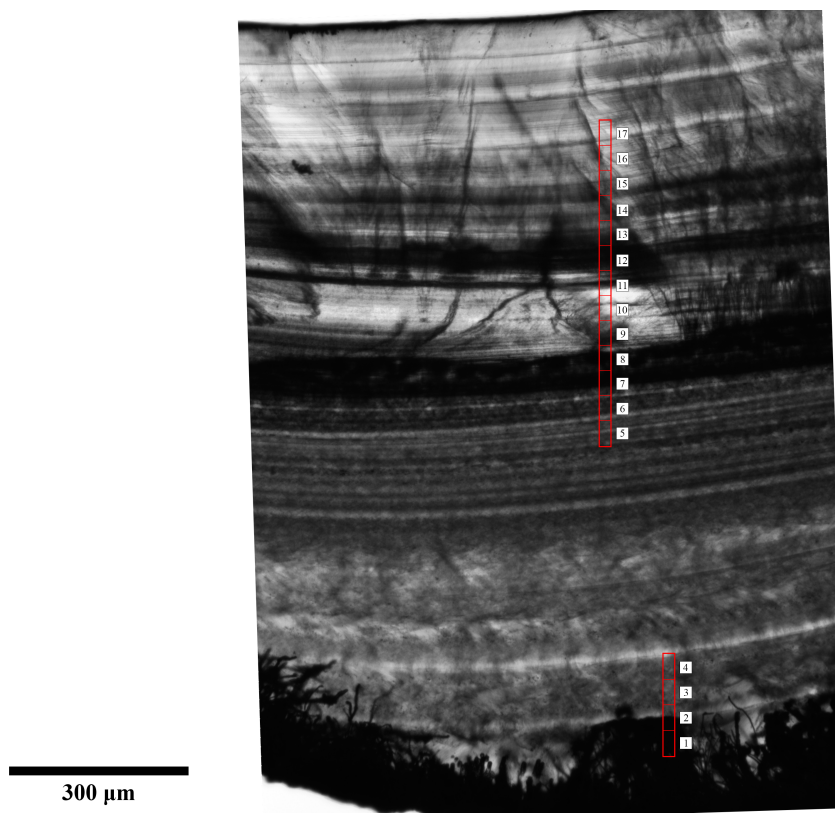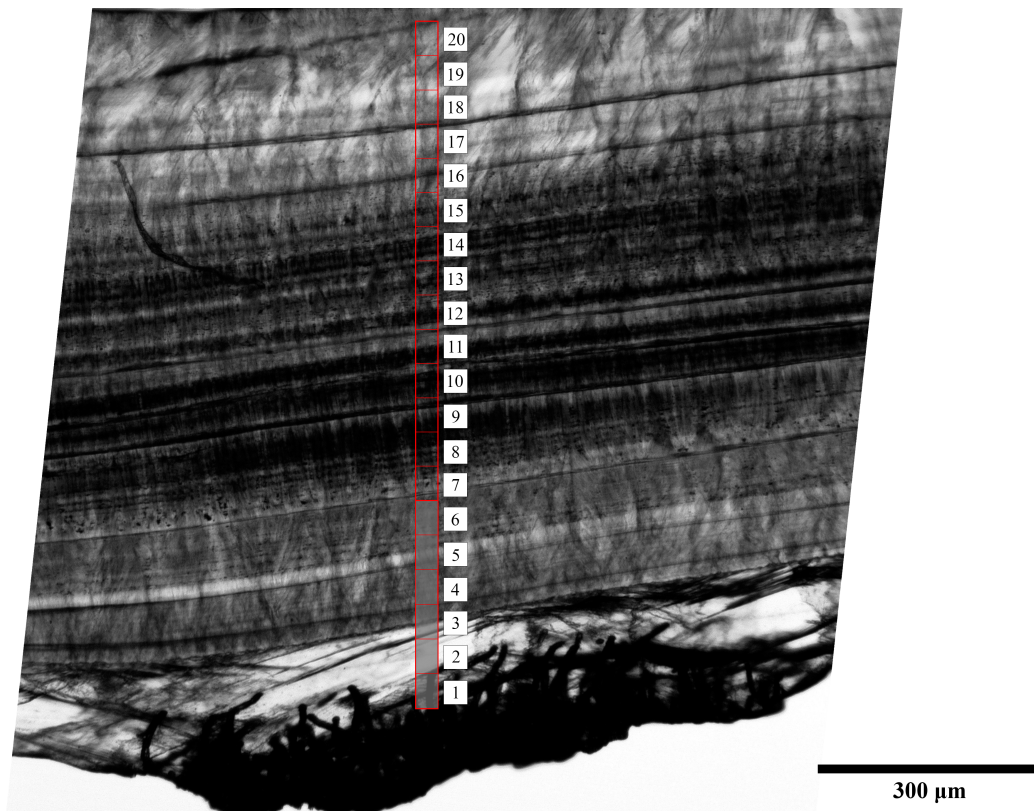
Figure 3.6: Sample Z1 visualized with optical microscope 50x enlargement. Red rectangles define the areas analyzed with XRF. Labels identify the different XRF maps. The gray area identify the maps that went lost during the acquisition.

3.2.   Samples for nano-tomography technique

One sample of *Patella caerulea*[3] was prepared for tomography analysis using the same shell utilized for sample G0 for XRF technique discussed in section 3.1. Nevertheless, the sample was prepared following a different procedure. Indeed, this techniques allowed to obtain information about the inner structure of the sample by retrieving its 3D mass density distribution. Compared to XRF analysis the sample sizes were increased to probe a larger volume, obtaining more information. The size of the sample is only limited by the incident X-ray beam, which is partly absorbed by the sample. Increasing the size of the sample provides a lower intensity at the position-sensitive camera deteriorating the signal. A size of 400 μm per side was considered a perfect compromise between volume of the sample probed and attenuation of the beam. The goal was to prepare a sample with a square cross section ($\approx 400 \cdot 400 \ \mu m^2$) including all the shell's width, from the periostracum to the inner shell layer. The region selected was the apex of the shell, consistently with the samples prepared for nano-XRF.

The sample preparation could be divided in two procedures. The first procedure consisted in preparing the same thin shell samples as described in section 3.1, with the only difference being that the sample thickness desired was 400 μm (thickness is here intended along the z direction as reported in Figure 3.3). Once the 400 μm thin shell sample was obtained, the second procedure was executed as described in the following.

The thin sample was embedded in acrylic resin again, as shown in Figure 3.7. Since the goal was to prepare a sample with squared cross section, both grinding and polishing procedures were performed along the x direction referring to Figure 3.7. The procedures followed for grinding and polishing were the same described in section 3.1. Once the sample thickness obtained was 400 μm along the x direction, another cleaning process with the ultrasonic bath was performed. The remaining resin attached to the sample was removed with the help of tweezers. Finally, the sample was mounted on the sample holder for nano-tomography, which consisted in a capillary made of glass of 0.5 mm in diameter, used as a support. The sample was attached on top of the capillary using a glue. The final sample ready for the analysis is reported in Figure 3.8.

3.2.1.   ROI identification for nano-tomography analysis

One sample of *Patella caerulea* was prepared for nano-tomography analysis (sizes $\approx 0.4 \cdot 0.4 \cdot 1.35 \ mm^3$) as described in section 3.2. Three single-distance tomography scan

---

[3]Samples were provided by our collaborator Youssef Lahbib, Université de Carthage, Faculté des Sciences de Bizerte
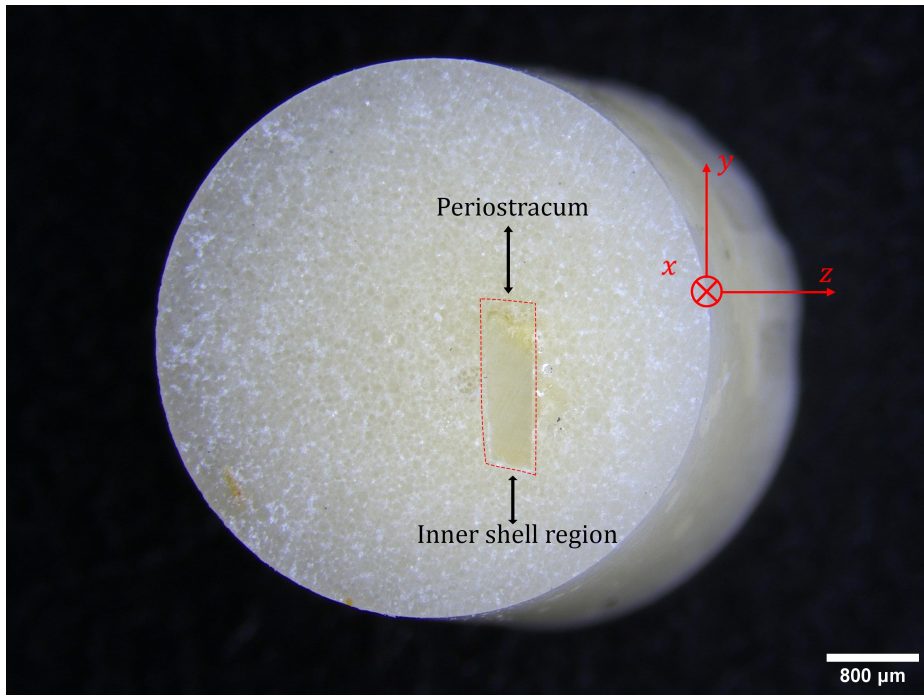
Figure 3.7: Top view of the thin shell film embedded in acrylic resin. The red dotted line identifies the edges of the samples embedded in the resin. The labels were introduced to better understand the sample orientation. The grinding procedure was then executed along the x direction. To better understand the orientation of the sample, a direct comparison can be done with Figure 3.3.

were performed covering the whole sample thickness, from the periostracum down to the shell inner layer, to get an overview of the whole sample, as shown in subsection 3.2.1. These three regions were named T, M and B, representing a Top region, a Middle region and a Bottom region inside the sample, respectively. These scans were performed with 241 nm voxel size, 20 ms exposure time and 3207 projections over 360°.

Three different Regions Of Interest (ROI) were then identified from the three scans with larger field of view: a top region (T_{ROI}), a middle region (M_{ROI}) and a bottom region (B_{ROI}). Thus, multi-distance (holographic tomography) scans were performed in these regions with 50 nm voxel size, 20 ms exposure time and 3207 projections over 360°.

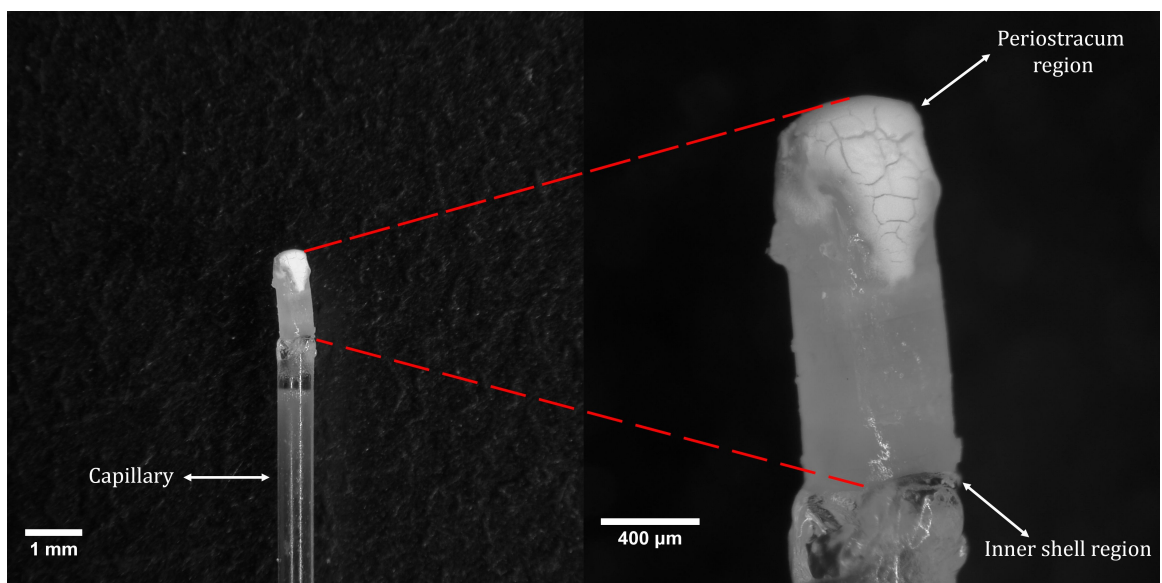Figure 3.8: Photograph of the sample prepared for nano-tomography analysis. The sample was attached on top of a capillary made of glass, used as a support. Labels help to identify the different regions of the sample. In the periostracum region could be noticed some resin still attached on it and not completely removed. Nevertheless, this was not considered a problem considering the working principle of nano-tomography technique.

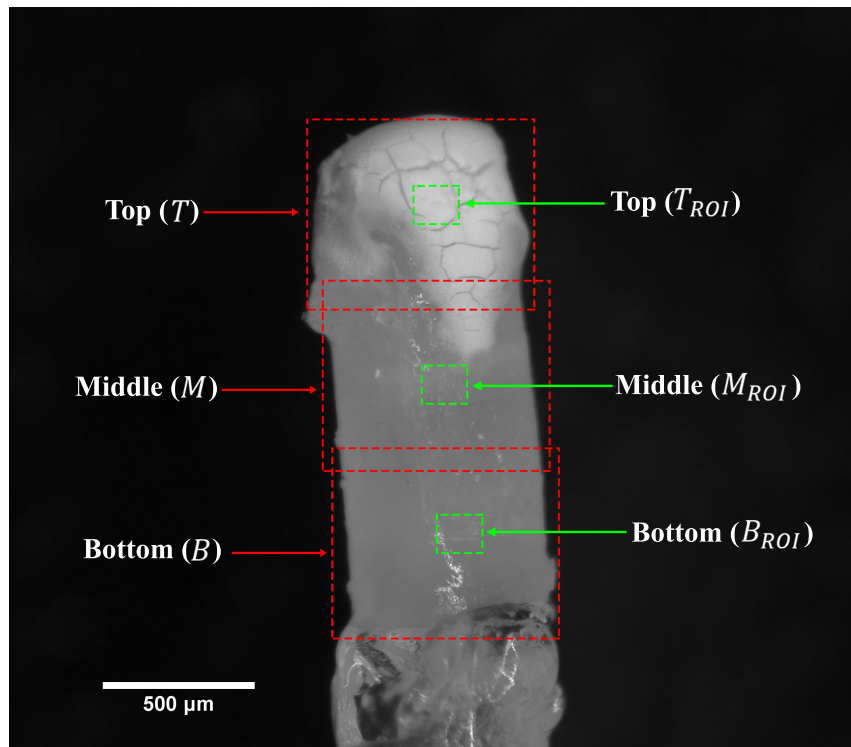Figure 3.9: Side view of the sample G0 prepared for tomography analysis. Red dotted lines identify the three scanned regions with 241 nm voxel size characterized by a large field of view. Green dotted lines identify the three ROIs scanned with higher resolution (50 nm voxel size). Labels were introduced to identify the different regions and to simplify the discussion of the results in chapter 4.

4 | Results and discussion

In the present study the composition of the shell of different samples of *Patella caerulea* was analyzed by means of nano-XRF and nano-tomography technique. More specifically, two samples from the polluted site of Gabes (G0 and G1) and one sample from the less polluted site of Zarat (Z1) were considered in the present study. Different regions of all the three samples were analyzed with XRF technique, while only one sample, coming from the Gabes site, was analyzed by nano-tomography.

At first, the analysis aimed to assess the global contamination of the samples, by identifying the average concentration of the main constituents together with trace metals incorporated in the shell structure. Subsequently, the nano-scale spatial resolution was fully exploited providing the chemical composition along the shell width. Further analysis were conducted along the shell width, possibly revealing changes of density in the shell structure correlated to the presence of trace metals. A separate discussion was dedicated to the interesting case of the outer layer of the shell, where an enhanced bioaccumulation was observed.

4.1. Assessing levels of pollution by comparison with literature

The vast majority of literature concerning biomonitoring studies provide the global elemental composition of the shell structure as a valid parameter for monitoring sea water quality [7, 16, 18, 20–22, 27]. More specifically, it is commonly reported a intra-study comparison where the chemical composition of different samples collected in different areas, among which a gradient of pollution is expected, are compared. The results reported in literature were considered for a possible inter-study comparison both to check whether the results obtained from XRF analysis were consistent with previous studies and to estimate the levels of pollution within the three sample of *Patella carulea*.

4.1.1. Major and minor components in the shell

The XRF spectrum of map 2 obtained from sample G0 and its fit, computed thourgh PyMCA, are reported in Figure 4.1.
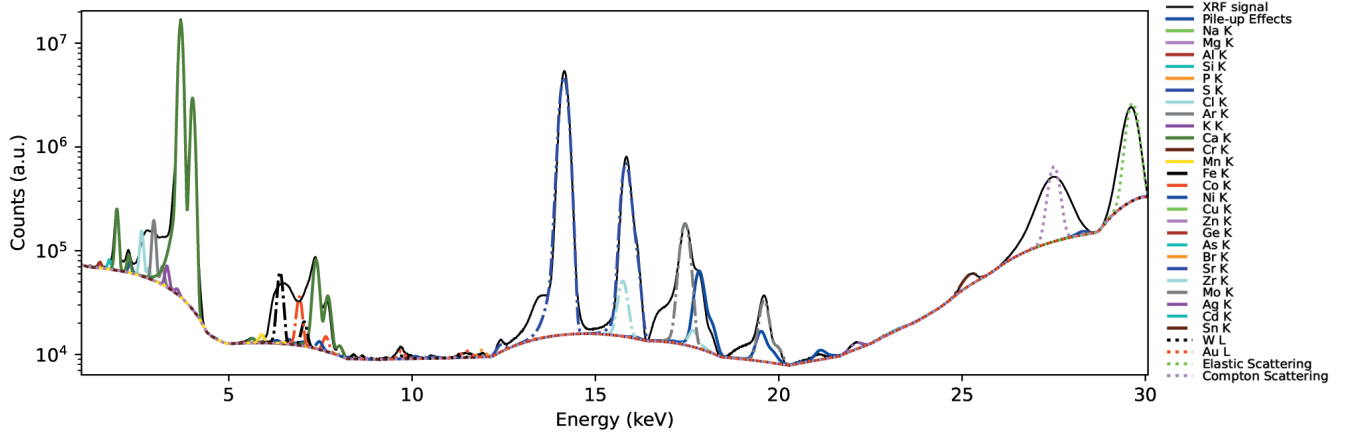

Figure 4.1: Results from fitting procedure from the XRF map 1 performed on sample G0.

The peaks associated to the main components (i.e., Ca and Sr) were clearly distinguishable. The peaks associated to Na ($K_{\alpha1} = 1040eV$), Mg ($K_{\alpha1} = 1253eV$), Al ($K_{\alpha1} = 1486eV$), Si ($K_{\alpha1} = 1739eV$), P ($K_{\alpha1} = 2013eV$), S ($K_{\alpha1} = 2307eV$) were also observed. However, quantification of these elements was not possible due to their low-energy emission lines, which lies below the strong Ca signal. Both C ($K_{\alpha1} = 277eV$) and O ($K_{\alpha1} = 525eV$), even though they represent the major components of the shell together with Ca, are characterized by emission lines too low in energy to be detected. Another strong emission peak around $17479\ eV$ could be observed in the spectrum which was associated to Mo, known to be part of the XRF detector composition. This prevented any possibility of assessing the real presence of this compound in the sample and it was considered only for the calibration procedure, as explained in subsection 2.3.3. Other features present in the spectrum were associated to the elastic scattering of X-rays ($E_{elastic} = 29.6keV$) and the inelastic Compton scattering ($E_{Compton} = 27.5keV$). Additional peaks were observed and ascribed to the presence of high concentration of some elements like Ca and Sr which give rise to pile-up effects. These peaks were correctly accounted during the fitting procedure.

The average concentrations were computed considering the concentration obtained for each XRF map. Maps overlapping the periostracum region were not included in the quantification, considering a possible enhanced bioaccumulation of trace elements due to direct exposure of this region to the surrounding environment [13–15]. A topic further

discussed in section 4.3. Maps from 1 to 7 of sample Z1 were not correctly saved during the measurement process, thus were not available for the present analysis. The concentrations obtained are reported in Table 4.1.

	G0	G1	Z1
Ca(%)	31.4 ± 0.4	27.3 ± 1	29.1 ± 0.5
Sr	1192.4 ± 79.0	1058.9 ± 168.0	1283.1 ± 113.7
Fe	215.4 ± 3.7	182.0 ± 7.2	196.3 ± 2.6
Cr	138.7 ± 1.5	132.1 ± 1.5	134.3 ± 0.9
Co	99.7 ± 1.6	84.3 ± 2.8	91.0 ± 1.1
Ni	98.5 ± 1.8	81.6 ± 3.2	89.3 ± 1.2
Mn	93.3 ± 1.3	85.4 ± 1.1	89.0 ± 0.5
Sn	43.5 ± 0.2	36.4 ± 0.2	45.7 ± 0.2
Cu	17.2 ± 0.3	15.9 ± 0.2	16.6 ± 0.1
Cd	13.3 ± 0.2	11.5 ± 0.2	14.0 ± 0.2
Zn	9.6 ± 0.1	8.9 ± 0.2	9.5 ± 0.1
W	7.9 ± 1.3	5.9 ± 0.6	6.6 ± 0.4
Ag	5.8 ± 0.1	4.8 ± 0.1	6.0 ± 0
Br	4.9 ± 0.1	4.5 ± 0.2	5.2 ± 0.1
As	4.7 ± 0.1	4.1 ± 0.2	4.6 ± 0.1
Ge	4.0 ± 0.1	3.7 ± 0.1	3.9 ± 0.1
Zr	2.2 ± 0.2	3.4 ± 1.5	3.4 ± 0.2

Table 4.1: Average chemical composition of the three samples analyzed expressed in $[\frac{\mu g}{g}]$. The reported standard deviation represents the variability among the different XRF maps considered for quantification. Red labels identified samples from the most contaminated site.

Levels of Ca ($27.3\% - 31.4\%$) lay within the range of values reported from different studies, where the concentration varies from $\approx 25\%$ in Nunez al. [19] up to $\approx 40\%$ in Slama et al. [18] considering shells coming from uncontaminated sites. This first observation suggested that results were consistent with the average values expected. As introduced in subsection 1.5.3, an overall decrease of Ca was observed for a variety of species of mollusks exposed to contaminated water, down to values of 8% [18], even though Begliomini et al. [22] reported a Ca content in shells coming from the polluted site of 31%. This suggested that different species of mollusks respond differently to the presence of pollution. Thus, a significant direct comparison could be made with other studies assessing

the chemical composition of the shell of the same species considered in the present study, namely *P. caerulea*. Unfortunately, no other such studies were found in literature. A comparison with other species belonging to the genus of *Patella* represented the most significant comparison that could be made. Nevertheless, no Ca alterations in the shell composition due to pollution were reported in literature for any *Patella* species.

No strong decrease of Ca was observed in the present study, even though a weak decreasing trend was still noticed, showing G0>Z1>G1. The order shown by G0 and Z1 hinted a possible higher pollution of sample Z1, considering the results reported in literature. Otherwise, this results could be interpreted as a different response mechanism of *P. caerulea* to pollution: Ca levels could increase in this species after exposure to a contaminated environment. Nevertheless, this second explanation was considered improbable. Considering sample G1, it was noticed that besides Ca, many other elements ranging from Sr to Ag (following the decreasing concentration in Table 4.1) showed a suspicious lower concentration compared to both G0 and Z1. The lower values obtained for G1 were possibly related to the specific region chosen in this sample. Indeed, it has to be noticed that maps ranging from 8 to 11 in sample G1 (Figure 3.5) were set on purpose to overlap a specific region where a self-repairing process seemed to occur. This region was thought to possibly provide interesting results from nano-scale analysis. Thus, a second quantification on sample G1 was performed neglecting this region, but the concentration obtained still provided lower values for this sample. Another possible explanation accounting for the lower values obtained for Ca, Sr, Fe, Cr, Co, Ni, Mn and Sn, was possibly related to the different thickness of sample G1 ($\approx 90~\mu m$) compared to the other samples G0 and Z1 ($\approx 60~\mu m$). An increase in thickness is associated to stronger self-absorption processes, possibly altering the results. Even though PyMca software provide the possibility to account the sample thickness for a correct quantification, it could be preferred to consider a batch of samples with homogeneous thickness for more significant quantification analysis. In conclusion, the concentrations obtained for G1 were not considered reliable.

Considering the concentration of Sr ($1058.9 - 1283.1~^{\mu g}/_g$) reported in Table 4.1, the values obtained for all the samples lied within the expected range of concentrations reported in literature for different species of mollusks (950 - 3500 $^{\mu g}/_g$) [27]. Possible alterations in Sr content, as previously mentioned in subsection 1.5.3, were related to contamination. More specifically, different species of *Patella* reported different behavior concerning Sr concentration . In *P. vulgata* [28] was observed an increase after contamination exposure, while *P. aspera* [27] showed the opposite behavior. Thus, no specific trend was expected for *P. caerulea*.

The results provided a decreasing trend following the order Z1>G0>G1. A direct compar-

ison among sample G1 and the other samples was considered poorly significant considering the previous discussion. Thus, considering only samples G0 and Z1, it was observed an opposite trend compared to Ca concentration. More specifically, Ca concentration was higher in G0, while Sr was higher in the Z1. The discording results reported in literature made difficult to draw solid conclusions concerning Sr.

Considering both Ca and Sr, no conclusion could be drawn regarding levels of pollution in the samples. The results reported lied in the expected typical values of concentration for these compounds, at least suggesting the meaningfulness of the results from quantification.

The concentration of trace elements could represent a more direct proof of the presence of pollution, compared to the assessment of possible variation of major constituents like Ca and Sr. Nevertheless, more sophisticated techniques and experimental apparatus are usually needed for quantifying trace elements.

As a last reminder, the quantification for sample G1 provided results considered suspicious and possibly related to the different thickness of this sample. For this reason, the results concerning this samples were neglected throughout the following analysis. Differently, samples G0 and Z1 were both considered for inter-studies and intra-study comparisons.

4.1.2. Trace metals concentration in the shell

Elements like Fe, Cu, Zn and Mn were considered essential for the mollusk, and were thus naturally present in the shell. Comparing the values obtained for these elements with studies on *Patella sp.*[1], levels of Fe were almost five times higher for both Z1 and G0 ($196.3 - 215.4 \, \mu g/g$), than the concentrations reported by Cravo et al. [27] ($44.9 \, \mu g/g$) for *P. aspera* collected from a polluted site. Cu levels ($16.6 - 17.2 \, \mu g/g$) were nearly eight times higher than those reported by Foster et al. [28] ($3.6 \, \mu g/g$) from contaminated samples, while levels of both Mn ($89.0 - 93.3 \, \mu g/g$) and Zn ($9.5 - 9.6 \, \mu g/g$) were approximately two times higher than values reported by Foster et al. [28] ($57.3 \, \mu g/g$ for Mn and $4.1 \, \mu g/g$ for Zn), thus giving a first proof of possible presence of contamination in all the samples analyzed.

Considering the intra-study comparison, for all the essential elements sample G0 showed a slightly higher concentration, except of Zn, compared to Z1. These results were thought to reflect the higher contamination of sample G0. Nevertheless, other en-

---

[1] *sp.* stands for species

vironmental factors should be taken into account whenever the aim is to correlate environmental contamination and presence of pollutant in the shell structure, as discussed in section 1.5, especially for essential elements which are naturally present in the shell. Additional shell parameters should be accounted whenever different samples are compared (e.g., the stage of life of the mollusk, sex) as in the present study. For instance, Cravo et al. [27] showed that smaller shells samples from a less contaminated site showed higher levels of Zn compared to the polluted site, in contrary to the result found for adult samples. Cravo et al. [27] explained this counter intuitive result by considering that during early stages of growth, mollusks selectively incorporate Zn in higher concentration in the shell structure. This mechanism would work more efficiently in uncontaminated samples, thus giving higher concentrations from the control site. During growth, the environmental availability plays a major role in further incorporation of this element, which led to an enhanced increase in contaminated samples compared to free from contamination ones. Another study [53]observed mollusk size-dependence for bioaccumulation of trace metals suggesting a higher uptake of Cd, Cr, Cu and Zn in soft tissues of adult samples of $P.$ $caerulea$. Thus, whenever selecting the batch of samples to analyze, the stage of life of the mollusks should also be taken into account, preferentially choosing a homogeneous set. In the present analysis, none of these parameters was considered, possibly influencing the results.

Compared to essential elements, the presence of non essential metals is mostly dictated by environmental availability. Thus, presence of these elements was considered to offer more straightforward conclusions concerning the level of pollution within a sample, even though a minor role is also played by other environmental conditions and other parameters (e.g., stage of life of the mollusk). No studies related to bioaccumulation of toxic metals in the shell structure for $Patella$ $sp.$ were found in literature, thus, the following discussion considered studies performed on different species of mollusks for comparison.

Cr concentrations reported in Table 4.1 ($134.3 - 138.7$ $\mu g/g$) were higher compared to the results reported from different studies [18,20,22], while being of the same order of magnitude reported in only one study on $Lottia$ $subrugosa$ [21] (254.9 $\mu g/g$), samples collected in a contaminated site. Thus, a possible Cr contamination of the samples was suggested, also supported by the elevated concentration of this element in PGF and the wide presence of tanneries along the litoral of the gulf.   The presence of Co in shell structure was poorly documented in literature, reported only by Almeida et al. [20], where presence of this element was found in samples of $Oysters$ shells. The present analysis reported concentrations almost seven times higher of Co ($91.0 - 99.7$ $\mu g/g$) suggesting a possible

contamination. Such results seemed in agreement with the water chemical composition from the gulf reported by Drira et al. [9], which showed presence of this compound, mainly attributed to phosphate industries waste products.

Levels of Ni ($89.3 - 98.5$ $\mu g/g$) were higher than those reported in two different studies [7, 18], considering samples both collected in uncontaminated and contaminated sites, with the smallest concentration reported to be 3.6 $\mu g/g$. Contrarily, Gouveia et al. [21] and Begliomini et al. [22] reported higher concentration both for samples coming from the contaminated and uncontaminated sites, with values up to 386.0 $\mu g/g$ in Begliomini et al [22]. These findings made hard to draw any conclusion about Ni levels. Nevertheless, Drira et al. [9] reported high concentration of this element in sea water collected in the vicinity of the city of Gabes, thus possibly suggesting that the concentration obtained represented a significant contamination from Ni.

Sn was detected in all the three samples, with concentrations ranging from 45.7 $\mu g/g$ in Z1 up to 43.5 $\mu g/g$ in sample G0. No studies reported presence of Sn in seashell composition, which could be attributed to the lower LOD of the different experimental techniques employed, compared to synchrotron radiation XRF. Moreover, considering the significant concentration of Sn observed in the shells, the low amount of this element in PGF composition suggested that its presence was possibly ascribed to TBT contamination of the water.

The values reported for Cd ($14.0 - 13.3$ $\mu g/g$) were significantly lower once compared to Gouveia et al. [21] and Begliomini et al. [22], that reported much higher concentrations in different samples up to a maximum value of (916.9 $\mu g/g$). Drira et al. [9] analyzed the concentration of different metals in sea water collected in the vicinity of Gabes, reporting significantly lower concentrations of Cd compared to other trace metals considered, thus suggesting a weak contamination from Cd in this area. Such results could justify the values reported in in the present study for this element.

El-Sorogy et al. [7] reported wide ranges of values for Ag from different samples collected along a contamination gradient The values reported for Ag ($6.0 - 5.8$ $\mu g/g$) in Table 4.1 corresponded to the concentration obtained from the lowest contaminated site in El-Sorogy et al. [7], where the highest concentration of Ag reported was 492 $\mu g/g$. Thus, Ag concentrations were not suggesting a strong contamination.

The same study [7] reported a constant concentration of As in all the shells among different sites with values (mean value of 1.55 $\mu g/g$) being approximately one third of the value obtained in the present study ($4.6 - 4.7$ $\mu g/g$).

Other elements such as W ($6.6 - 7.9$ $\mu g/g$), Br ($5.2 - 4.9$ $\mu g/g$), Ge ($3.9 - 4.0$ $\mu g/g$) and Zr ($3.4 - 2.2$ $\mu g/g$) were detected in all the three samples. Presence of W, Br, Ge and Zr in shell structure are poorly documented in literature, nonetheless Slama et al. [18]

reported presence of W and Zr in samples of *Siphonaria pectinata*. The values of concentrations reported by Slama et al. [18] were twenty times higher (166 $\mu g/g$) and five times higher (12.1 $\mu g/g$), respectively, compared to the values obtained in the present study. The presence of these two compounds was still ascribed to PGF contamination.

In conclusion, the concentrations reported for essential trace metals were suggesting a possible contamination in in both sample G0 and Z1. Indeed, the values reported in all samples were higher than values found in literature for all Fe, Cu, Zn and Mn. Considering an intra-study comparison, sample G0 showed a slightly higher accumulation of these elements compared to Z1, suggesting higher contamination for this sample.

The concentrations found for different non-essential metals hinted a possible significant accumulation compared to other studies. In particular, elements like Cr, Co, Sn, showed higher concentrations than those found in literature from different mollusk species [18, 20, 22]. In contrary, levels of Cd, Ag, were significantly lower than values reported by other studies from samples collected in contaminated sites [7, 20–22]. For the remaining elements (i.e., Ni, As, W, Br, Ge, Zr) no conclusions were drawn from the inter-studies comparison.

Considering an intra-study comparison for non-essential metals, sample G0 showed a slightly larger accumulation of Cr, Co, Ni and W, while a slightly larger accumulation of Sn and Zr was shown for sample Z1. The remaining non essential elements (i.e., Cd, Ag, Br, As and Ge) showed approximately the same concentrations between the two samples. The differences in concentration reported among G0 and Z1 were lower than the differences usually reported in literature from comparisons between samples from contaminated sites and samples from less contaminated sites. Indeed, most of the studies reported variation of one or two orders of magnitude in non essential metal concentrations [7, 18, 20–22]. This suggested that the contamination gradient between Gabes and Zarat was not high enough to promote significant chemical alterations.

4.2. Shell composition analysis with nano-scale resolution

Biomonitoring studies usually provide the overall chemical composition of the shell structure, considering both main constituents and trace elements, but without spatially resolving their distribution [7, 16, 18, 20–22, 27]. Other studies that reported the chemical composition resolved down to μ-scale [24, 25], only considered the major components of the shell stucture. No high resolution spatially resolved analysis concerning trace metals were found in literature. To enrich this poorly investigated topic the present section proposes a nano-scale spatially resolved analysis , showing elemental composition variations along the shell width of both major and minor constituents and trace elements. Additionally, possible inhomogeneities in the shell structure will be assessed relying on nano-tomography technique. The elemental distribution in the outer layer will be discussed in a separate section.

4.2.1. Distribution of major and minor constituents

The distribution of Ca showed a quite homogeneous distribution for both samples, being present in high concentration ($\approx$ 30% of shell composition) all along the shell width. This result was expected considering that $CaCO_3$ is the main component of the shell structure. Nevertheless, some stripes characterized by a lower Ca concentration (up to a 2% decrease) were observed in all the samples, with a simultaneous increase of Sr composition (up to 1800 $\mu g/g$), hinting a substitution. An example for the presence of these stripes is reported in Figure 4.2 where Ca and Sr distribution are reported from map 2 to map 22 for sample G0.
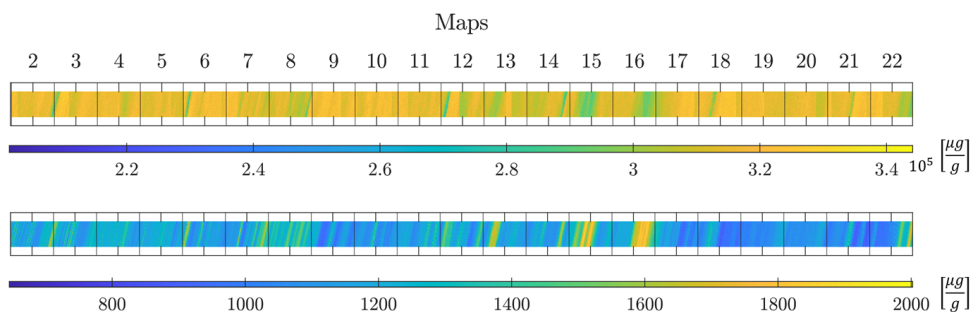

Figure 4.2: XRF maps of sample G0 for Ca on top and Sr at the bottom. The maps are reported rotated compared to sample orientation showed in Figure 3.4. Map 1 was neglected in the present analysis and further considered in section 4.3.

These observations were consistent with studies on *Patella sp.* [54] and other gastropods [25], which showed an increase of Sr and S in concomitance of what were defined as growth lines (or growth increments). The growth lines are located at interfaces between consecutive layers formed during the shell growth and were also observed in the optical microscope images reported in Figure 3.4, Figure 3.5, Figure 3.6.

The growth lines were also observed in the nano-tomography scans performed in T region (in M and B regions as well), as reported in Figure 4.3. Nevertheless, considering the higher concentration of Sr in these regions reported by the XRF analysis, the tomography analysis was expected to reveal a higher density within these regions. Instead, the intensity in concomitance of growth lines compared to the bulk of the shell (Figure 4.3) suggested either the presence of inner-pores or possibly an abundant concentration of lighter elements not detectable with XRF (such as C, S, P and Mg), other than Sr, which possibly decreased the overall density within these regions.
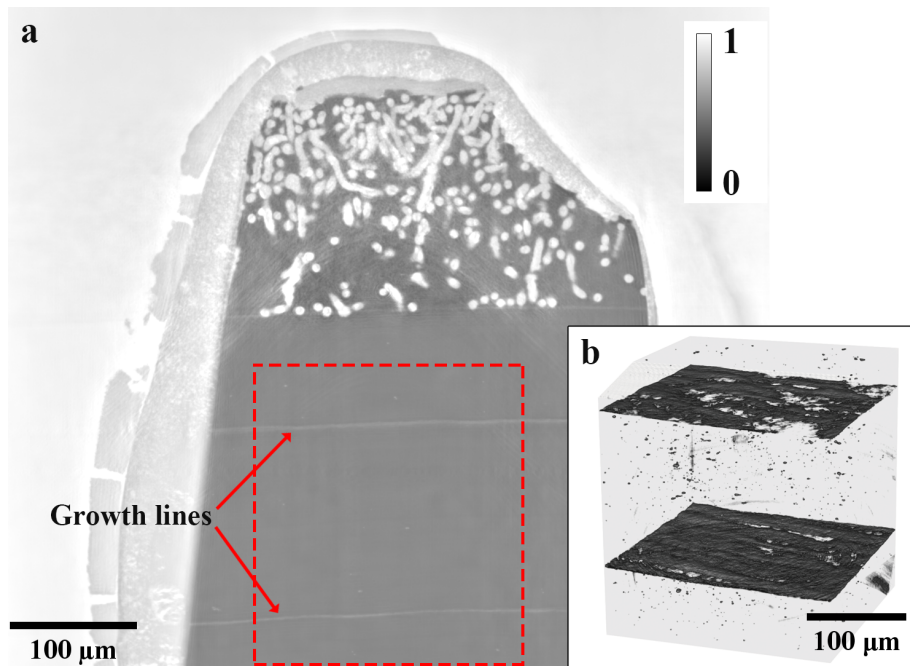

Figure 4.3: Nano-tomography scan from the T region. Bright regions represent a less dense structure while dark regions represent a more dense structure in (a). (a) Side view of the inner shell structure. The red dotted rectangle identifies the sub-volume selected for the 3D rendering. (b) 3D rendering showing two consecutive growth lines in dark. The threshold was set to avoid displaying the denser $CaCO_3$ bulk. Other spherical features observable in the rendering were interpreted as porosities. In the bottom right corner of the rendering could be identified a larger feature representing background noise.

Another way to visualize the possible $Ca - Sr$ substitution, is presented in Figure 4.4

where it was compared the spatial distribution of Ca and Sr averaged over horizontal lines of the XRF maps(i.e., along the direction of the growth lines). Whenever a Ca content decrease was observed, a concomitant increase of Sr was identified, as highlighted by the black arrows in the Figure 4.4.
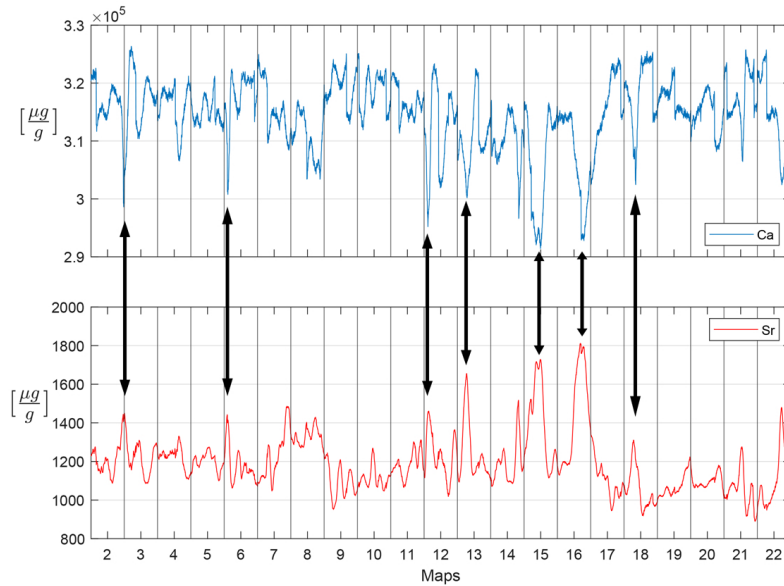

Figure 4.4: Spatial distribution of Ca and Sr in sample G0. The values represent the average concentration computed over horizontal lines (i.e., parallel to the growth lines). Black arrows highlight regions where Ca and Sr showed an opposite variation in concentration, suggesting a substitution.

This result suggested to assess a possible substitution among Ca with other elements, which might be present but not as evident as in the case of Ca-Sr. Thus, a Pearson correlation analysis was performed for both samples (G0 and Z1), considering a correlation between Ca and all the other elements as reported in Figure 4.5.

The correlation was performed by the use of MATLAB software relying on the built-in function *corrcoef* [55]. Additionally, the correlation was computed considering all the pixels from the XRF maps. The results showed a significant anti-correlation with Sr ($r_{G0} = -0.62$, $r_{Z1} = -0.64$) compared to the values reported for the other elements, corroborating the Ca-Sr substitution previously suggested. Nevertheless, other trace elements reported a correlation coefficient r different from zero, as better discussed in the following subsection.
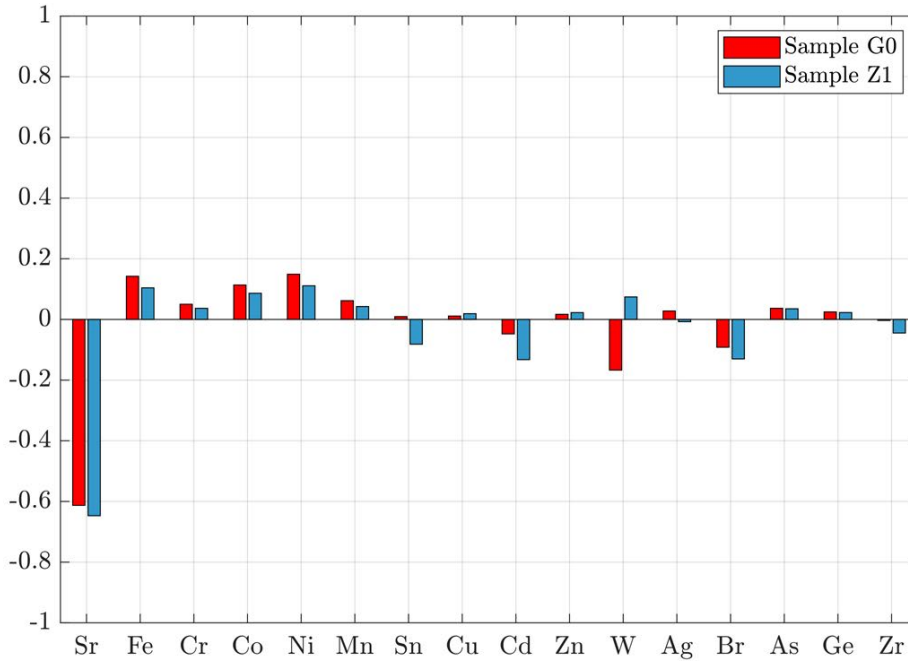
Figure 4.5: Results from Pearson correlation analysis between Ca distribution and all the other elements. The correlation was computed relying on the built-in function *corrcoef* implemented in MATLAB [55]. Strong anti-correlation was obtained with Sr in all the samples compared to the weaker correlation of other elements.

4.2.2. Trace elements distribution

Considering the results from the correlation analysis, other elements like Sn ($r_{Z1} = -0.08$), Cd ($r_{G0} = -0.05, r_{Z1} = -0.13$), W ($r_{G0} = -0.17$), Br ($r_{G0} = -0.09$, $r_{Z1} = -0.13$) and Zr ($r_{Z1} = -0.04$) showed an anti-correlation with Ca, even though much weaker compared to Sr. A more a accurate inspection of XRF maps showed a enhanced concentration for elements with $r \leq -0.09$ (except for Cd) in concomitance of the growth lines, corroborating a substitution with Ca, even though less evident than Sr. Thus, it was concluded that W for sample G0 and Br for both samples showed an enhanced concentration in concomitance of growth lines, as shown in Figure 4.6.
The other elements characterized by a correlation coefficient such that $-0.09 < r < 0$, didn't show any appreciable inhomogeneous distribution from a direct inspection of the XRF maps, suggesting that the negative correlation obtained was possibly a result of the background noise in the XRF maps and that those elements were instead dispersed homogeneously in the shell.

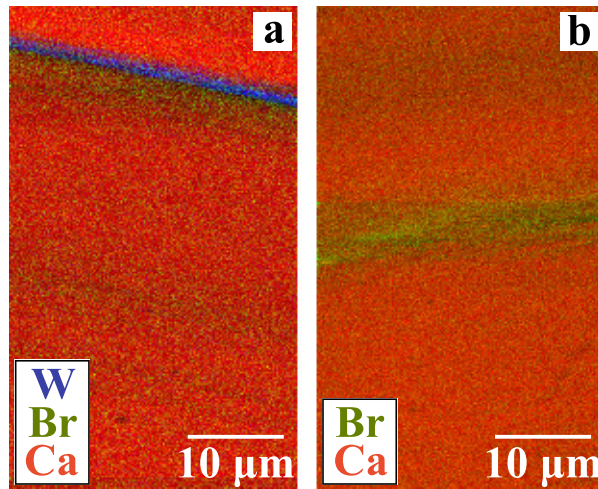Other elements reported a correlation coefficient $r \geq 0$, such as Cr, Mn, Ni, Co, Ge .

Figure 4.6: XRF maps showing presence of Br and W in the shell. (a) represent the XRF map $n°14$ of sample G0. (b) represents the XRF map $n°16$ from sample Z1.

Nevertheless, no distinguishable features were observed from the XRF maps. Contrarily, Cu, Fe, Sn, Zn and Ag were, characterized by a $r \geq 0$ (with the exception of Sn for which $r_{Z1} = -0.08$), showed a homogeneous background distribution together with the presence of different localized regions with higher concentration of these elements. An example for sample G0 is reported in Figure 4.7. No specific pattern about the localization along the shell width of these agglomerates was observed.
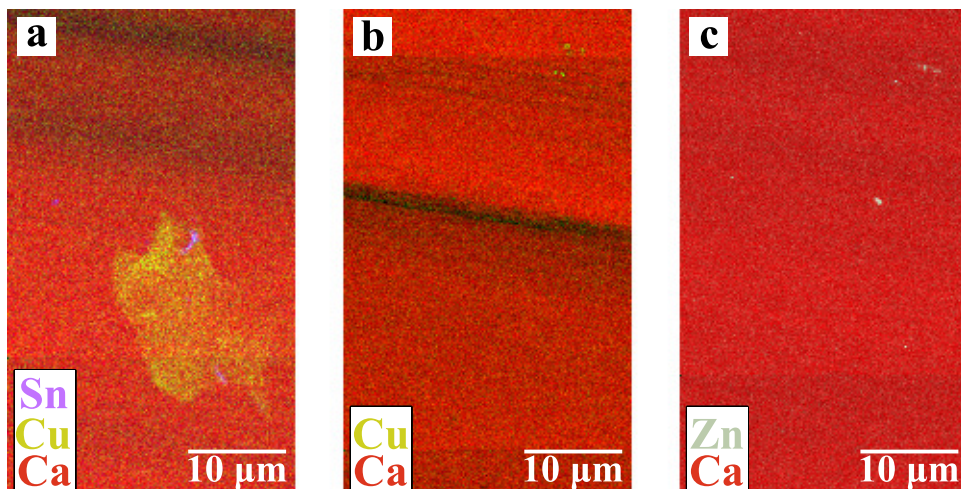

Figure 4.7: Elemental distribution maps of sample G0 after XRF fitting. Ca concentration is represented in red. (a) Map 22 reported presence of high-concentration regions of Cu and Sn. (b) Map 21 reported presence of high-concentration regions of Cu. (c) Map 11 reported presence of high-concentration regions of Zn.

The localized regions ranged in sizes from 200 nm up to ≈ 20 μm and their presence

was double checked with two different SSD detectors. Whenever such a feature was observed in only one of the two detector it was discarded, since it was considered a possible artefact. These regions were manually measured from the XRF maps. A summary of these high-concentration regions is reported in Figure 4.8.
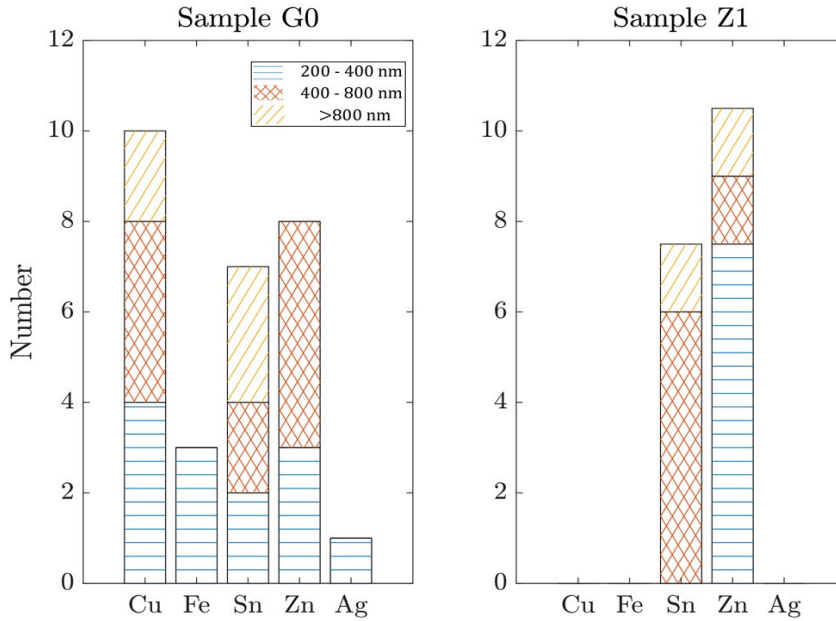

Figure 4.8: Bar plot reporting the number of high-concentration regions identified in different samples for different elements. These features were grouped depending on their spatial extension. The values were rescaled considering the larger area analyzed of samples G0 compared to Z1. Thus, values for sample G0 were those effectively observed, while the numbers obtained for sample Z1 where multiplied by a factor $\frac{Area_{G0}}{Area_{Z1}}$. This allowed a direct comparison between the samples. The elements are reported following the decreasing concentrations reported in Table 4.1.

Considering that the total area probed for the two samples was different, the values reported in Figure 4.8 were rescaled. In particular, the number of high-concentration regions reported for sample G0, were those effectively observed, while the numbers obtained for sample Z1 where multiplied by a factor $\frac{Area_{G0}}{Area_{Z1}}$. In this way a direct comparison between samples was possible.

High-concentration regions for Cu were identified in G0, showing different sizes, while no features were observed for Z1 concerning this element. This result could possibly be explained assuming that G0 was more polluted compared to Z1 concerning this element, as also supported by previous analysis. Lopes-Lima et al. [8] suggested the kidney as the active extrection pathaway for Cu adopted in $A.\ cygnea$. Nevertheless, a high contam-

ination could have induced excretion in the shell structure as well, for sample G0. The lower contamination to which Z1 was exposed possibly allowed a correct excretion of the excess Cu involving only the kidney. Thus, the mollusk could have exploited the shell as an excrection mechanism for active detoxification for the excess of Cu, resulting in the formation of such regions.

Similarly to Cu, Fe was considered as an essential element, always present in the shell. The formation of high-concentration regions of 200 - 400 nm size, present only in G0 could be accounted considering these samples as the most polluted ones. Nevertheless, no suggestions regarding the main excretion mechanism exploited by *P. caerulea* for this elements were found in literature.

High-concentration regions were observed for Zn in all the samples. Sample G0 showed a higher tendency to present larger size regions compared to sample Z1, characterized by mostly 200-400 nm size regions. As suggest by Lopes-Lima et al. [8] high accumulation of Zn in the mollusk would induce an active detoxification process through the shell. This was considered the possible reason of why high-concentration regions for this element were found in both samples.

High-concentration regions of Sn were observed in both samples G0 and Z1. More specifically, sample G0 showed an heterogeneity concerning the sizes of these area. In contrary, Z1 analysis mainly showed regions with sizes comprehended in the 400 - 800 nm range.As previously mentioned, no studies were found in literature concerning presence of Sn in the shell structure. This was possibly associated to the lower LOD provided by the commonly used techniques compared to synctrontron radiation XRF.

The presence of high concentration of Ag in localized regions was reported only in sample G0. The absence in sample Z1 could be explained by assuming a smaller environmental contamination from Zarat site for this element. Croteau et al. [12] reported the tendency of the gastropod *Lymnaea stagnalis* to bioaccumulate both Ag^+ and Ag nanoparticles in soft-tissues after controlled exposure. In particular, the direct uptake of nanoparticles in soft-tissues could possibly lead to an incorporation of these agglomerated in the crystal structure. This was though to possibly account for the presence of these high-intensity regions observed for Ag and for all the other metals.

No other studies concerning localized trace metals in shell structure were found in literature.

4.2.3.   Presence of nano and micro pores in the shell structure

Nano-tomography analysis was expected to possibly reveal presence of trace metals agglomerates in the bulk region of the shell, corroborating the results from XRF analysis. Instead, the inner bulk region of the shell was characterized by spherical nano and microscale low-density regions, as shown in Figure 4.9.
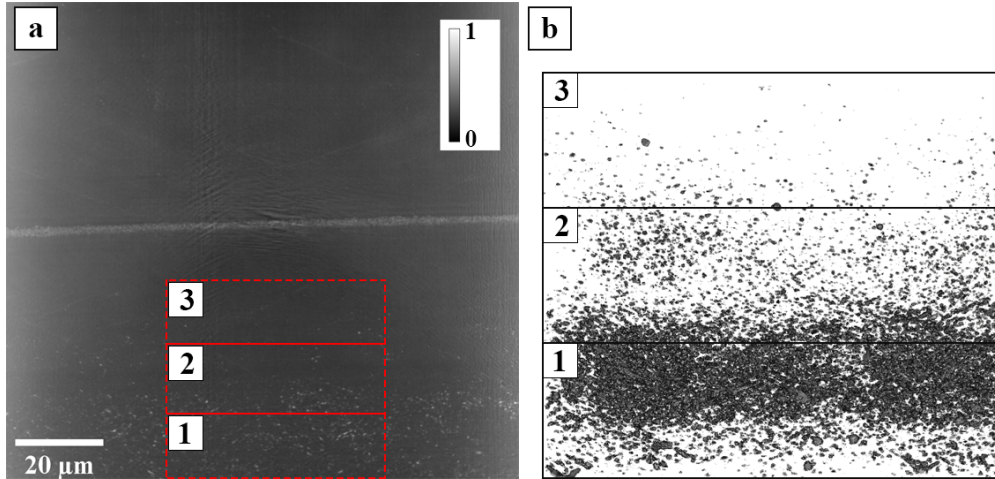

Figure 4.9: Nano-tomograhy scan from region M_{ROI} with 50 nm resolution. (a) A side view of the inner structure of the shell is shown. Bright intensity represents low density regions, dark intensity represents high density regions. The red dotted rectangle identifies the volume selected for further analysis. Labels 1, 2 and 3 identify three different sub-volumes of $50 \cdot 50 \cdot 15 \mu m^3$. A higher concentration of low-density regions resembling pores was identified in the bottom part, more specifically in volume **1**. (b) A 3D rendering showing the results from the segmentation procedure. The pores sizes and concentration were analyzed within the three different sub-volumes 1, 2 and 3. Results are reported Figure 4.10

These features were considered as pores, and possibly related to an erroneous mineralization, consequence of environmental stress. As shown in Figure 4.9.a the distribution of the pores was not homogeneous inside the structure, identifying regions with an enhanced concentration. To better quantify the inhomogeneity, the volume identified with red dotted lines in Figure 4.9.a was segmented by setting a threshold, to extrapolate the pores from the background, as shown in Figure 4.9.b. The pores were then labeled exploiting ImageJ software. The labelling procedure allowed to index the pores. Subsequently, the pores volume was computed exploiting ImageJ plugin *3D Analysis*, setting a three dimensional connectivity of 26 and excluding the pores on the edges. This volume considered for the analsis was subdivided into three different sub-volumes as shown in Figure 4.9.b. Both pores number and sizes were decreasing significantly moving from volume **1** to volume **3**,
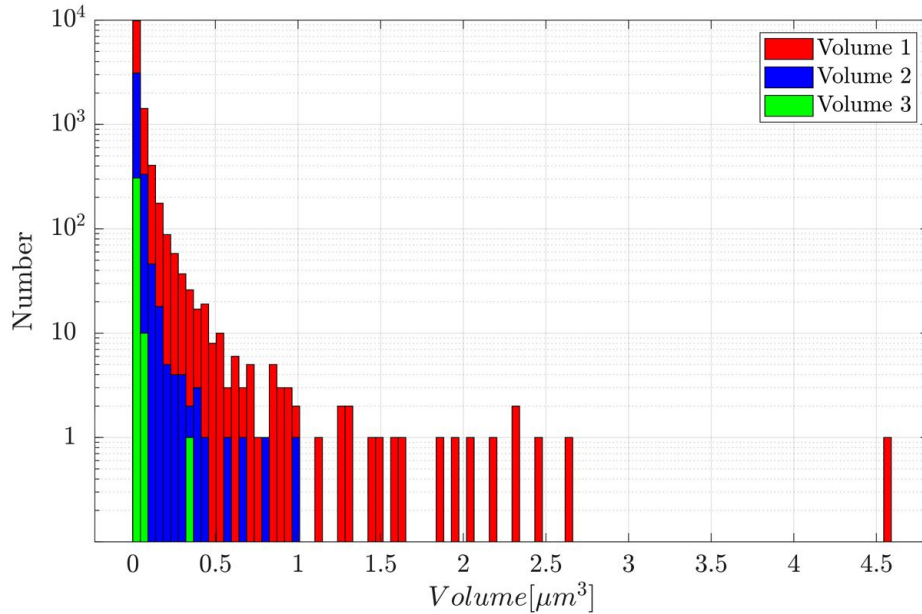
as can be observed in Figure 4.10

Figure 4.10: Histogram plot reporting the distribution of the sizes of the pores within each of the three sub-volumes introduced in Figure 4.9. The pores were grouped in bins of $450\mu m^3$. Volume 1 reported more numerous and larger pores, followed by volume 2 and finally volume 3, where pores were smaller and fewer.

The presence of more numerous and larger pores in volume **1** suggested that at specific times during the growth of the calcified layer, the mollusk suffered from environmental stress. This hypothesis was elaborated considering the finding of Chang-Yu et al. [6] who reported presence of micro and nano-pores at the growth surface of coral skeletons, which probably follow a similar biomineralization process with respect to mollusks [3]. The pores identified at the growth surface were suggested to be later filled through a IA mechanism, by Ca^{2+} ions. Possibly, environmental stressors such as contamination might interfere in this process and avoid the filling of the pores. Nevertheless, other factors were a possible cause of environmental stress, such as changes in water temperature, salinity or pH. If pollution was the source of environmental stress causing of formation of pores, a higher concentration of trace metals was possibly expected in volume **1**, compared to volume **3**. In this way, rather than directly detecting the trace metals dispersed in the shell, the effects of the contamination could be detected, namely, the formation of pores.

Further analysis should be conducted to assess the possible correlation among trace metals accumulation and presence of porosities.

In conclusion, the distribution of major and minor components, i.e., Ca and Sr, showed inhomogeneities associated to the presence of growth lines, already observed in literature [25,54]. In particular, a $Ca-Sr$ substitution was observed within these regions, also supported by the Pearson correlation analysis. Other elements such as W for sample G0 and Br for both samples, showed an enhanced concentration in concomitance of these regions, suggesting a substitution with Ca again supported by the Pearson correlation analysis, even though less pronounced once compared to Ca-Sr substitution.

Nano-tomography scans showed an overall decrease in density in concomitance of the growth lines, possibly suggesting that beside Sr, W and Br other light elements were highly accumulated in these regions, not observed through XRF because of the their low emission lines. This hypothesis was congruent with the finding of Dauphin et al [25] and Nouet et al. [54] where both S and Mg accumulation was observed in concomitance of the growth lines. An alternative hypothesis, considered, rather than light elements accumulation, the presence of fibrous porosities in concomitance of the growth lines, which would have decreased the overall density of these regions.

Trace elements as Cr, Mn, Ni, Co, Ge and Zr didn't shown any distinguishable feature inside the maps, also corroborated by the weak correlation obtained with Ca. These elements were thus considered to be homogeneously dispersed within the $CaCO_3$ matrix. Other elements such as Cu, Fe, Sn, Zn and Ag showed a homogeneous background distribution together with the presence of different localized regions with higher concentration of these elements. This fact was not expected considering the results of the correlation analysis. The localized regions ranged in sizes from 200 nm up to ≈ 20 μm, and didn't show any specific trend regarding their location. Considering the essential metals, Zn agglomerates were present in both samples, while Cu and Fe were identifies only in the samples coming from the most polluted site. Regarding non-essential metals, Sn agglomerates were found both in samples G0 and Z1, while Ag agglomerates were detected only in sample G0. These results also supported the expected stronger contamination of sample G0.
The presence of these features for different metals was though to be associated to a direct uptake of sub-μm size metal particles. Indeed, Croteau et al. [12] reported a direct uptake of Ag nanoparticles in the soft-body of a species of gastropod. We assumed that a subsequent excretion in the shell could possibly lead to the incorporation of these metallic nanoparticles for the elements observed, even though these findings were not reported by any other study. Exploiting a lower spatial resolution for XRF and considering more samples could provide further insight regarding the metal agglomerates identified in the present study.

The nano-tomography analysis perfomed with 50 nm spatial resolution in the bulk

of the shell, didn't show any of such metallic agglomerates, making questionable their real presence. An hypothesis was elaborated to possibly account for their absence in nano-tomography scans. These agglomerated could be regions were metals were accumulated as nanoparticles with sizes smaller than the spatial resolution achieved with nano-tomography and dispersed together with other elements. XRF would be more sensitive to the presence of metals finely dispersed with other elements than nano-tomography, which is only sensitive to local changes in density. In this case, nano-tomography would provide only an average density of the regions where metallic nanoparticles were accumulated, and possibly the small variation in density was buried in the background noise. Nano-tomograhy results could be improved by employing more powerful reconstruction algorithms compared to the iterative algorithm exploited. This would reduce noise and allow to achieve higher sensitivity to local variation in density. This will possibly reveal metallic nanoparticles, corroborating the finding from XRF technique.

Unexpectedly, nano-tomgraphy scans showed presence of pores inside the bulk of the shell, with a inhomogeneous distribution and possibly related to an erroneous mineralization. In particular, the presence of pores could be associate to a failure of the filling mechanism of Ca^{2+} suggested by Chang-Yu et al [6], assumed to be caused by environmental stress. If the source of environmental stress was pollution we were expecting to observe a concomitant accumulation of trace metals in the region where more numerous and larger pores were observed. Nevertheless, a first qualitative comparison among trace metals concentration and pores distribution didn't shown any evident correlation. Further analysis should be performed to rigorously assess a possible correlation.

4.3.   Elemental distribution in the outer layer

The outermost layer of the seashell, i.e., the periostracum, is known to possibly accumulate trace elements by direct exposure with the external environment [13–15]. A direct analysis on this peculiar shell layer could provide further insights regarding the enhanced bioaccumulation already reported in literature for different species.

A first look to the XRF maps performed on the outer layer region suggested the presence of distinctive features. Indeed, specific regions within the maps showed a lower Ca signal, resembling the presence of holes in the shell structure as shown in Figure 4.11. These features observed in the XRF maps were also noticed from the microscope images (Figure 3.4, Figure 3.5, Figure 3.6) supporting the hypothesis that the periostracum region

presented cavities. Similar findings were reported by different studies [17,54] where microscope images from the outer layer showed cavity-like features associated to microfouling activity.
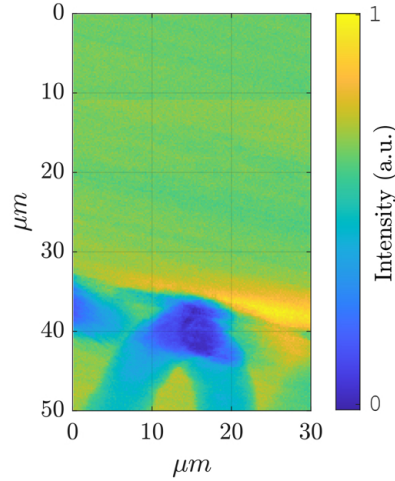

Figure 4.11: XRF map from the periostracum regions for Ca. The figure represents map 1 from sample G0. The intensity of the maps was normalized. Lower Ca concentration regions, represented in blue, hinted the possible presence of cavities in this outer layer where an enhanced accumulation of trace elements could occur.

A clear evidence of the presence of cavities was observed by means of nano-tomography scans in concomitance of the periostracum. A 3D rendering of a sub-volume of the scan in the T region, showed the presence of low density regions resembling cavities, as shown in Figure 4.12.

The XRF spectra measured in these regions showed, together with a decrease in Ca concentration, an enhanced accumulation for some trace elements. As an example, in Figure 4.13 are shown two XRF spectra coming from Map 1 of sample G0. The upper spectrum was obtained from the whole map, while the bottom spectrum was obtained from the XRF signal coming only from the regions where cavities were identified. The fitting procedure allowed to determine which elements were mostly accumulated inside the cavities as shown in Figure 4.14. In particular, the elements which showed an increase in the emission lines intensities were Fe, Co, Ni, Cu, Zn, W, Br and Ge for sample G0 ($Fe_{K\alpha1} = 6400\ eV, Co_{K\alpha1} = 6930\ eV, Cu_{K\alpha1} = 8047\ eV, W_{L\alpha1} = 8397\ eV, Zn_{K\alpha1} = 8638\ eV, Ge_{K\alpha1} = 9886\ eV, As_{K\alpha1} = 10543\ eV, Br_{K\alpha1} = 11924\ eV, Rb_{K\alpha1} = 13395\ eV$). Elements like Fe, Co, Ni, Cu and Zn were found to be abundant both in the inner shell bulk, as showed in subsection 4.1.1, and in the cavities. Other elements such as W, Br and Ge were present in the shell structure at low concentration compared to the elements
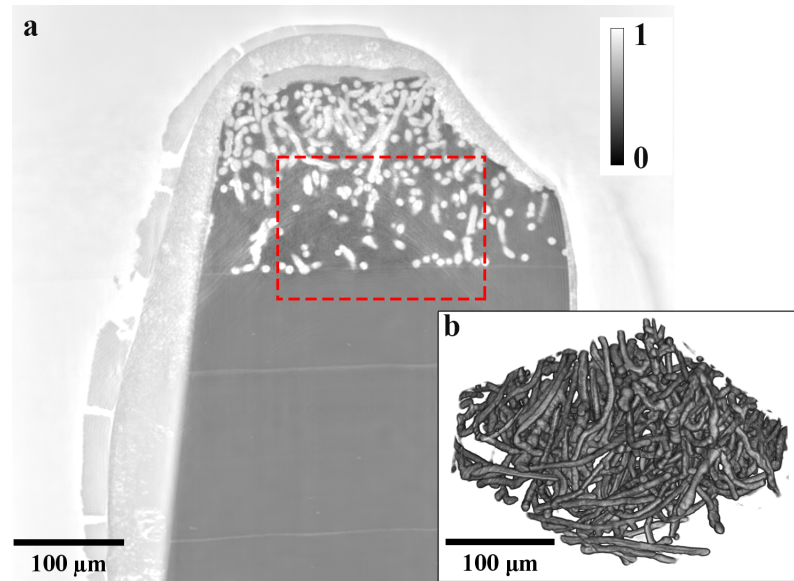
Figure 4.12: Nano-tomography scan from T region. (a) Single slice showing the inner shell structure. Bright regions correspond to a less dense structure, while darker regions represent denser part of the shell. The red dotted rectangle identifies the sub-volume selected for the 3D rendering ($193 \cdot 134 \cdot 193 \ \mu m^3$). (b) 3D rendering showing the presence of cavity-like features. The threshold was set to only display these less dense regions and not to the denser $CaCO_3$ matrix.

just mentioned, while being present in the cavities in higher concentrations. Thus, a possible discussion for W, Br and Ge considered a scarce uptake of these elements by the mollusk, explaining the small concentrations found in the shell bulk. On the other side, the environmental availability promoted accumulation in the outer layer by surface adsorption and diffusion into the cavities.

The results from nano-tomography scans performed with 50 nm resolution showed a inhomogeneous density inside the cavities, as reported in Figure 4.15. This possibly suggested that the cavities walls were characterized by a different composition, being more dense, compared to the inner regions, which were assumed to be an empty volume. The denser regions could possibly contain the trace elements detected from XRF analysis. Nevertheless, as can be noticed in Figure 4.15 the background mainly composed of $CaCO_3$ was denser than the cavities walls, suggesting that no heavy metals could be identified in these regions. A possible explanation, which would support the presence of trace metals in the cavities walls, was associated to the different sensitivity of XRF technique and nano-tomography. XRF technique is considered more sensitive to low concentration of trace metals being a chemical composition sensitive technique. Nano-tomography provides
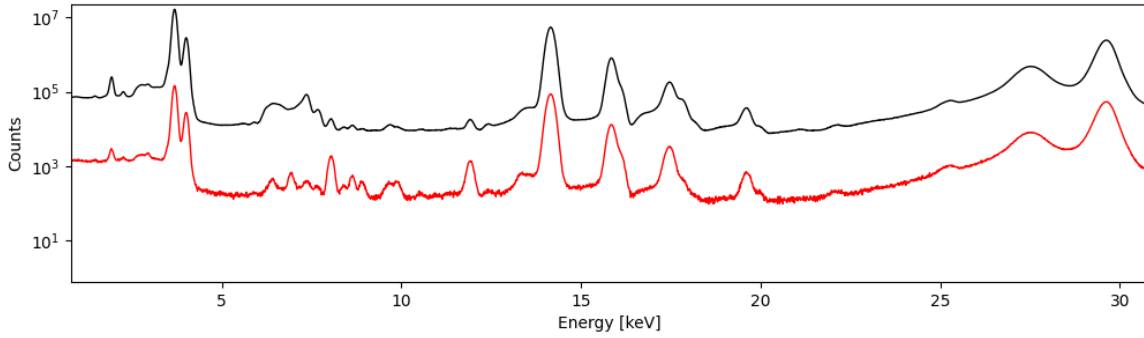
Figure 4.13: XRF spectra obtained from Map 1 of sample G0. The upper curve represents the whole spectrum associated to Map 1. The bottom curve was obtained by selecting only the signal coming from the region where cavities were identified. The major differences could be noticed in concomitance of different energies $(6400\ eV, 6930\ eV, 8047\ eV, 8397\ eV, 8638\ eV, 9886\ eV, 10543\ eV, 11924\ eV, 13395\ eV)$.
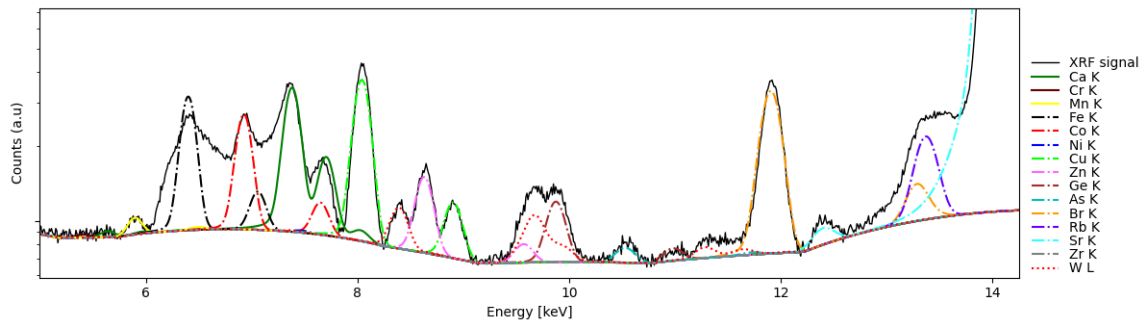

Figure 4.14: Results from the fitting performed on the bottom spectrum showed in Figure 4.13. The specific interval of energies shown was considered the most interesting one, where a noticeable increase of different peaks could be observed compared to the top spectrum of Figure 4.13. The increased intensities suggested a stronger accumulation for Fe, Co, Ni, Cu, Zn, W, Br and Ge in the cavity regions present in the periostracum.

information regarding the density of the sample, and could show the presence of heavy metals only if those were dispersed as nanoparticles larger than the spatial resolution ($50\ nm$). Assuming heavy metals to be dispersed homogeneously in the cavities walls with other light elements, such as Mg and S [17, 54], would possibly provide an average density of the structure lower than the one of $CaCO_3$.

In conclusion, XRF technique showed an enhanced accumulation of trace metals inside the cavities present in the periostracum region, as already suggested by different studies [13–15]. As shown in the present study, a variety of elements could accumulate
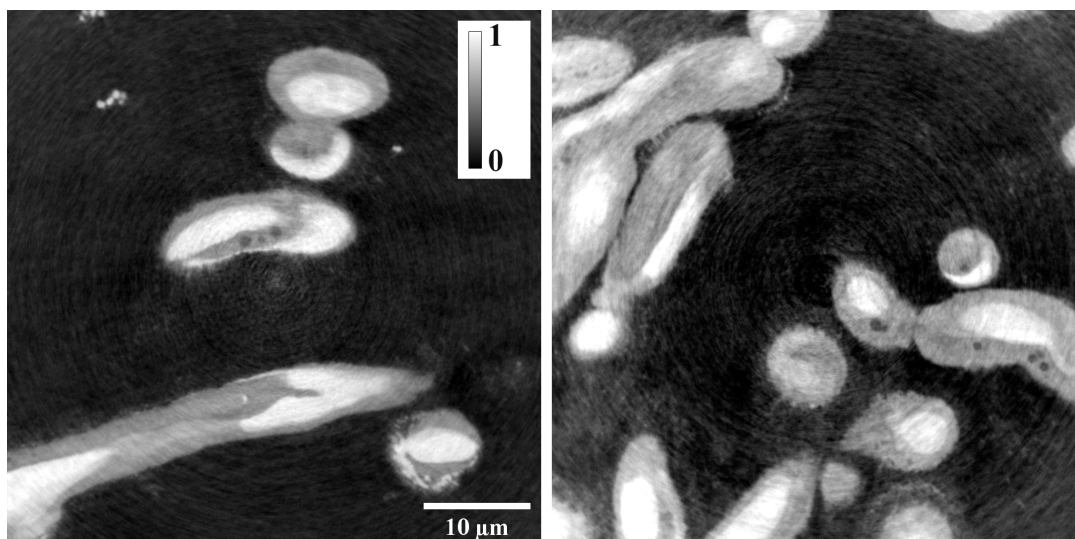
Figure 4.15: Two different slices from the nano-tomography scan performed in the T_{ROI} region with 50 nm of resolution. The images showed a different composition inside the cavities. The white regions were assumed to be empty volume regions. The light-grey regions were suggested to represent the walls of the cavities. The ring-like shape present in the background of the image is an artefact.

in this region making it suitable for biomonitoring purposes, even though low LOD techniques might be required. Nano-tomography analysis confirmed that these regions could effectively be considered as cavities, characterized by a inhomogeneous inner composition. Nevertheless, no direct proof of the presence of trace metals were identified by the nano-tomography scans. This was possibly associated to the different sensitivity of this technique once compared to XRF, whenever trace metals are finely dispersed with other elements. Further analysis could be performed with nano-tomography technique exploiting more powerful reconstruction algorithms to reduce the noise and possibly obtain higher resolution images.

5 | Conclusions

In the present study two samples of seashells of *Patella caerulea* were analyzed by means of nano-XRF and nano-tomography technique. A first analysis, concerning an overall quantification of the chemical composition employing XRF technique, revealed a slight higher contamination by trace metals in sample G0 collected from the harbor area of Gabes, compared to sample Z1, collected in Zarat sites. A contamination gradient was reported among those sites, congruent with the results from quantification.

The nano-scale spatially resolved analysis with XRF showed a Ca-Sr substitution in concomitance of different growth lines, also supported by a correlation analysis. Similarly, Br and W had the tendency to accumulate in this region. Nano-tomography analysis reported a decrease in density, with respect to the $CaCO_3$ bulk, in concomitance of growth lines, in contrary to the expected increase associated to Sr, Br and W accumulation. This result was either suggesting the presence of inner porosities within growth lines or possibly an abundant concentration of light elements, not detectable with XRF, which would have decreased the overall density within these regions.

The nano-scale resolution also revealed the presence of metal agglomerates for Cu, Fe, Sn, Zn and Ag dispersed in the shell of the most polluted sample, while only Sn and Zn agglomerates were reported in the less polluted one. The presence of these metallic nano and micro-agglomerates possibly suggested a direct uptake of metallic nanoparticles by the mollusk with a subsequent excretion in the shell structure. No specific distribution along the shell width was observed for these metallic agglomerates. Further analysis considering more samples and different regions of the shell could provide a more significant statistics concerning metals agglomerates distribution.

Nano-tomography analysis was expected to possibly reveal the presence of trace metals agglomerates in the bulk region of the shell, corroborating the results from XRF analysis. Nevertheless, no such findings were reported from nano-tomography analysis. Instead, the inner bulk region of the shell was characterized by nano and micro-scale pores. The distribution was inhomogeneous, and regions characterized by more numerous and larger pores were identified. Environmental stressors, such as pollution, were hypothesized to interfere with the correct mineralization process and induce a enhanced formation of pores,

detrimental for the mechanical properties of the shell structure. If pollution was the cause of the enhanced pores formations, a possible correlation was expected among pores and trace metals distribution within the shell structure. A first qualitative comparison didn't shown any evident correlation. Further analysis should be performed to rigorously assess a possible correlation.

A separate analysis was focused in the outer layer of the shell, showing a enhanced accumulation for different trace metals such as Fe, Co, Ni, Cu, Zn, W, Br and Ge. The elemental distribution of Ca in the outer layer hinted the presence of micro cavities, also corroborated by nano-tomography analysis, associated to biofouling activity within this region. The morphology of this layer together with its direct exposure to sea water justified the enhanced heavy metals accumulation observed. No findings regarding metal accumulation in the cavities were suggested by nano-tomography results, possibly related to the different sensitivity of this technique compared to XRF. Considering the tendency of the periostracum to accumulate different trace metals, its chemical composition could be employed as a valid parameter for biomonitoring studies.

Bibliography

[1] Raymond S. Bradley. *Paleoclimatology: Reconstructing Climates of the Quaternary.* Academic Press, third edition edition, 2015.

[2] Benjamin Marie Frederic Marin, Nathalie Le Roy. The formation and mineralization of mollusk shell. *FBS*, 4(3):1099–1125, 2012.

[3] Pupa U. P. A. Gilbert, Kristin D. Bergmann, Nicholas Boekelheide, Sylvie Tambutté, Tali Mass, Frédéric Marin, Jess F. Adkins, Jonathan Erez, Benjamin Gilbert, Vanessa Knutson, Marjorie Cantine, Javier Ortega Hernández, and Andrew H. Knoll. Biomineralization: Integrating mechanism and evolutionary history. *Science Advances*, 8(10):eabl9653, 2022.

[4] A. Valeria Bers, Fraddry D'Souza, Job W. Klijnstra, Peter R. Willemsen, and Martin Wahl. Chemical defence in mussels: antifouling effect of crude extracts of the periostracum of the blue mussel mytilus edulis. *Biofouling*, 22(4):251–259, 2006.

[5] Kevin Kocot, Felipe Aguilera, Carmel McDougall, Daniel Jackson, and Bernard Degnan. Sea shell diversity and rapidly evolving secretomes: Insights into the evolution of biomineralization. *Frontiers in Zoology*, 13, 06 2016.

[6] Chang-Yu et al. Sun. From particle attachment to space-filling coral skeletons. *Proceedings of the National Academy of Sciences of the United States of America*, 2020.

[7] Abdelbaset El-Sorogy, Ahmed El Kammar, Abdelmohsen Ziko, Mohsen Aly, and Hamdy Nour. Gastropod shells as pollution indicators, red sea coast, egypt. *Journal of African Earth Sciences*, 87:93–99, 2013.

[8] Manuel Lopes-Lima, Susana Freitas, Liliana Pereira, Eugenia Gouveia, Mariana Hinzmann, Antonio Checa, and Jorge Machado. Ionic regulation and shell mineralization in the bivalve anodonta cygnea (swan mussel) following heavy-metal exposure. *Canadian Journal of Zoology*, 90(2):267–283, 2012.

[9] Zaher Drira, Houda Sahnoun, and Habib Ayadi. Spatial distribution and source identification of heavy metals in surface waters of three coastal areas of tunisia. *Polish Journal of Environmental Studies*, 26, 05 2017.

[10] M. Zaidi, K. Athmouni, I Metais, and et al. The mediterranean limpet patella caerulea (gastropoda, mollusca) to assess marine ecotoxicological risk: a case study of tunisian coasts contaminated by metals. *Environmental Science and Pollution Research*, 29, 2022.

[11] Yang Du, Fei Lian, and Lingyan Zhu. Biosorption of divalent pb, cd and zn on aragonite and calcite mollusk shells. *Environmental Pollution*, 159(7):1763–1768, 2011.

[12] Marie-Noële Croteau, Superb K. Misra, Samuel N. Luoma, and Eugenia Valsami-Jones. Silver bioaccumulation dynamics in a freshwater invertebrate after aqueous and dietary exposures to nanosized and ionic ag. *Environmental Science & Technology*, 45(15):6600–6607, 2011.

[13] Michael Zuykov, Emilien Pelletier, Richard Saint-Louis, Antonio Checa, and Serge Demers. Biosorption of thorium on the external shell surface of bivalve mollusks: The role of shell surface microtopography. *Chemosphere*, 86(6):680–683, 2012.

[14] U. Sturesson. Lead enrichment in shells of mytilus edulis. *Ambio*, 5(5/6):253–256, 1976.

[15] J.H. Swinehart and K.W. Smith. Iron and manganese deposition in the periostraca of several bivalve mollusks. *Biological Bulletin (Woods Hole)*, (Woods Hole):369–381, 1979.

[16] Maximiliano Cledón. Laitano María V., Jesús D. Nuñez. Shell alterations in the limpet bostrycapulus odites: A bioindicator of harbour pollution and mine residuals. *Ecological Indicators 34*, 2013.

[17] Lahbib Youssef, Slama Tasnime, Abidli Sami, Nouet Julius, Chassefière Eric, and Trigui El Menif Najoua. Shell alterations in hexaplex trunculus collected in the vicinity of an impacted zone by industrial marine discharges (gabès, southern mediterranean). *Journal of Sea Research*, 181:102178, 2022.

[18] Slama Tasnime, Nouet Julius, Chassefière Eric, Trigui El Menif Najoua, and Lahbib Youssef. Monitoring of coastal pollution using shell alterations in the false limpet siphonaria pectinata. *Marine Pollution Bulletin*, 173:113063, 2021.

[19] Jesús D. Nuñez, María V. Laitano, and Maximiliano Cledón. An intertidal limpet species as a bioindicator: Pollution effects reflected by shell characteristics. *Ecological Indicators*, 14(1):178–183, 2012.

[20] M.J Almeida, G Moura, T Pinheiro, J Machado, and J Coimbra. Modifications in crassostrea gigas shell composition exposed to high concentrations of lead. *Aquatic Toxicology*, 40(4):323–334, 1998.

[21] Nayara Gouveia, Carolina R.M. Oliveira, Camila P. Martins, Luciane A. Maranho, Camilo Dias Seabra Pereira, Manoela R. de Orte, Cyntia A.Y. Harayashiki, Sérgio M. Almeida, and Italo B. Castro. Can shell alterations in limpets be used as alternative biomarkers of coastal contamination? *Chemosphere*, 224:9–19, 2019.

[22] Felipe Nincao Begliomini, Daniele Claudino Maciel, Sérgio Mendonça de Almeida, Denis Moledo Abessa, Luciane Alves Maranho, Camilo Seabra Pereira, Gilvan Takeshi Yogui, Eliete Zanardi-Lamardo, and Ítalo Braga Castro. Shell alterations in limpets as putative biomarkers for multi-impacted coastal areas. *Environmental Pollution*, 226:494–503, 2017.

[23] Carolina Rocha Moreira Oliveira, Leandro Mantovani de Castro, Monick Alves da Cruz Nazareth, Cyntia Ayumi Yokota Harayashiki, and Ítalo Braga Castro. Shell structure and composition alterations in the limpet lottia subrugosa along a contamination gradient in the santos estuary, brazil. *Ecological Indicators*, 115:106417, 2020.

[24] Y. Dauphin, G. Luquet, M. Salome, L. Bellot-Gurlet, and J.P. Cuif. Structure and composition of unio pictorum shell: arguments for the diversity of the nacroprismatic arrangement in molluscs. *Journal of Microscopy*, 270(2):156–169, 2018.

[25] Yannicke Dauphin, Jean-Pierre Cuif, Marine Cotte, and Murielle Salomé. Structure and composition of the boundary zone between aragonitic crossed lamellar and calcitic prism layers in the shell of concholepas concholepas (mollusca, gastropoda). *Invertebrate Biology*, 131(3):165–176, 2012.

[26] Gregorio Bigatti and Pablo Penchaszadeh. Imposex in odontocymbiola magellanica (caenogastropoda: Volutidae) in patagonia. *Comunicaciones de la Sociedad Malacológica del Uruguay*, 9, 2005.

[27] A Cravo, P Foster, and M.J Bebianno. Minor and trace elements in the shell of patella aspera (röding 1798). *Environment International*, 28(4):295–302, 2002.

[28] P. Foster and J. Chacko. Minor and trace elements in the shell of patella vulgata (l.). *Marine Environmental Research*, 40(1):55–76, 1995.

[29] Radhouan El Zrelli, Pierre Courjault-Radé, Lotfi Rabaoui, Sylvie Castet, Sylvain Michel, and Nejla Bejaoui. Heavy metal contamination and ecological risk assessment in the surface sediments of the coastal area surrounding the industrial complex of gabes city, gulf of gabes, se tunisia. *Marine Pollution Bulletin*, 101(2):922–929, 2015.

[30] Neila Annabi-Trabelsi, Wassim Guermazi, Qusaie Karam, Mohammad Ali, Saif Uddin, Vincent Leignel, and Habib Ayadi. Concentrations of trace metals in phytoplankton and zooplankton in the gulf of gabès, tunisia. *Marine Pollution Bulletin*, 168:112392, 2021.

[31] Radhouan El Zrelli, Lotfi Rabaoui, Heithem Abda, Nabil Daghbouj, Rafael Pérez-López, Sylvie Castet, Thierry Aigouy, Nejla Bejaoui, and Pierre Courjault-Radé. Characterization of the role of phosphogypsum foam in the transport of metals and radionuclides in the southern mediterranean sea. *Journal of Hazardous Materials*, 363:258–267, 2019.

[32] Erik Ytreberg, Maria Alexandra Bighiu, Lennart Lundgren, and Britta Eklund. Xrf measurements of tin, copper and zinc in antifouling paints coated on leisure boats. *Environmental Pollution*, 213:594–599, 2016.

[33] Dimitris Vafidis, Irini Drosou, Kostantina Dimitriou, and Dimitris Klaoudatos. Population characteristics of the limpet patella caerulea (linnaeus, 1758) in eastern mediterranean (central greece). *Water*, 12(4), 2020.

[34] Tasnime Slama, Sami Abidli, Najoua Trigui El Menif, and Youssef Lahbib. Grazer gastropods as alternative species for monitoring butyltins contamination in harbors. *Journal of Sea Research*, 190:102287, 2022.

[35] T Yüzereroğlu, Gülbin Gök Feridun, H Coğun, Özgür Fırat, Sabahattin Aslanyavrusu, Onur Maruldali, and F Kargin. Heavy metals in patella caerulea (mollusca, gastropoda) in polluted and non-polluted areas from the iskenderun gulf (mediterranean turkey). *Environmental monitoring and assessment*, 167:257–64, 2009.

[36] ESRF. `https://www.esrf.fr/about`, 2023. [Online].

[37] ESRF. `https://www.esrf.fr/home/UsersAndScience/Accelerators/the-accelerator-complex.html`, 2023. [Online].

[38] A. Joly. Esrf highlights 2022. Technical report, ESRF, February 2023.

[39] Carlo Meneghini Settimio Mobilio, Federico Boscherini. *Synchrotron Radiation: Basics, Methods and Applications.* Springer, 2015.

[40] Jaime Segura with contribution from Julie Villanova and Remi Tucoulou. Manual for ID16 beamline named 'ID16B Beamline Review report - final.pdf'.

[41] ESRF. `https://www.esrf.fr/UsersAndScience/Experiments/XNP/ID16B`, 2023. [Online].

[42] D. M. Mills, J. R. Helliwell, Å. Kvick, T. Ohta, I. A. Robinson, and A. Authier. Report of the Working Group on Synchrotron Radiation Nomenclature – brightness, spectral brightness or brilliance? *Journal of Synchrotron Radiation*, 12(3):385, May 2005.

[43] Gema Martínez-Criado, Julie Villanova, Rémi Tucoulou, Damien Salomon, Jussi-Petteri Suuronen, Sylvain Labouré, Cyril Guilloud, Valentin Valls, Raymond Barrett, Eric Gagliardini, Yves Dabin, Robert Baker, Sylvain Bohic, Cédric Cohen, and John Morse. ID16B: a hard X-ray nanoprobe beamline at the ESRF for nano-analysis. *Journal of Synchrotron Radiation*, 23(1):344–352, Jan 2016.

[44] R. Jenkins, R. Manne, R. Robin, and C. Senemaud. `https://www.esrf.fr/home/UsersAndScience/Accelerators/the-accelerator-complex.html`, 1991. Nomenclature system for X-ray spectroscopy.

[45] Julie Villanova, Sabine Schlabach, Annabelle Brisse, and Aline Léon. X-ray fluorescence nano-imaging of long-term operated solid oxide electrolysis cells. *Journal of Power Sources*, 421:100–108, 2019.

[46] V.A. Solé, E. Papillon, M. Cotte, Ph. Walter, and J. Susini. A multiplatform code for the analysis of energy-dispersive x-ray fluorescence spectra. *Spectrochimica Acta Part B: Atomic Spectroscopy*, 62(1):63–68, 2007.

[47] The MathWorks Inc. Matlab version: 9.9.0 (r2020b), 2020.

[48] Anton Paar. `https://www.axo-dresden.de/fileadmin/axo/documents/products/reference/Prospekt_ReferenceSamples_2022-01_web.pdf`, 2021. [Online].

[49] David M. Paganin and Daniele Pelliccia. Chapter two - x-ray phase-contrast imaging: a broad overview of some fundamentals. In Martin Hÿtch and Peter W. Hawkes, editors, *Advances in Imaging and Electron Physics*, volume 218 of *Advances in Imaging and Electron Physics*, pages 63–158. Elsevier, 2021.

[50] P. Cloetens, Wolfgang Ludwig, José Baruchel, Dirk van dyck, J. Landuyt, Jean-Pierre Guigay, and M. Schlenker. Holotomography: Quantitative phase tomography with micrometer resolution using hard synchrotron radiation x rays. *Applied Physics Letters*, 75:2912 – 2914, 12 1999.

[51] Caroline Schneider, Wayne Rasband, and Kevin Eliceiri. Nih image to imagej: 25 years of image analysis. *Nature Methods*, 9, 07 2012.

[52] MATLAB. `https://fr.mathworks.com/help/images/ref/volumeviewer-app.html`, 2023. [Online].

[53] Francesco Cubadda, Marcelo Enrique Conti, and Luigi Campanella. Size-dependent concentrations of trace metals in four mediterranean gastropods. *Chemosphere*, 45(4):561–569, 2001.

[54] Julius Nouet, Corinne Chevallard, Bastien Farre, Gernot Nehrke, Emilie Campmas, Emmanuelle Stoetzel, Mohamed Abdeljalil El Hajraoui, and Roland Nespoulet. Limpet shells from the aterian level 8 of el harhoura 2 cave (témara, morocco): Preservation state of crossed-foliated layers. *PLoS ONE*, 10, 2015.

[55] MATLAB. `https://fr.mathworks.com/help/matlab/ref/corrcoef.html`, 2023. [Online].